Science of the Total Environment 969 (2025) 178982

Contents lists available at ScienceDirect

Science of the Total Environment

journal homepage: www.elsevier.com/locate/scitotenv

Leveraging synergies between UAV and Landsat 8 sensors to evaluate the impact of pale lichen biomass on land surface temperature in heath tundra ecosystems

Miguel Villoslada [a,b,1,*], Thaísa Bergamo [a,b,1], Tiina Kolari [c,d], Rasmus Erlandsson [e,f], Pasi Korpelainen [a], Aleksi Räsänen [g], Teemu Tahvanainen [d], Hans Tømmervik [e], Tarmo Virtanen [h], Emelie Winquist [i], Timo Kumpula [a]

[a] Department of Geographical and Historical studies, University of Eastern Finland, P.O. Box 111, FI-80101 Joensuu, Finland
[b] Institute of Agriculture and Environmental Sciences, Estonian University of Life Sciences, Kreutzwaldi 5, EE-51006 Tartu, Estonia
[c] Centre de recherche sur la dynamique du système Terre (GEOTOP), Université du Québec à Montréal, C.P. 8888, Succ. Centre-Ville, Montréal, QC, H3C 3P8, Canada
[d] Department of Environmental and Biological Sciences, University of Eastern Finland, P.O. Box 111, FI-80101 Joensuu, Finland
[e] Norwegian Institute for Nature Research (NINA), FRAM – High North Research Centre for Climate and the Environment, Tromsø, Norway
[f] Department of Ecology, Environment and Plant Sciences, Stockholm University, Sweden
[g] Geography Research Unit, University of Oulu, Oulu, Finland
[h] Ecosystems and Environment Research Programme, University of Helsinki, Helsinki, Finland
[i] University Centre in Svalbard, P.O. Box 156, N-9171 Longyearbyen, Svalbard, Norway

HIGHLIGHTS

- UAV and satellite data reveal cooling effects of pale lichens on Arctic land temperatures.
- Increased lichen biomass reduces land surface temperature, especially at the landscape scale.
- UAV models accurately predict fine-scale lichen biomass and vascular vegetation cover.
- Combining UAV and satellite data improves ecosystem monitoring at multiple spatial scales.

GRAPHICAL ABSTRACT

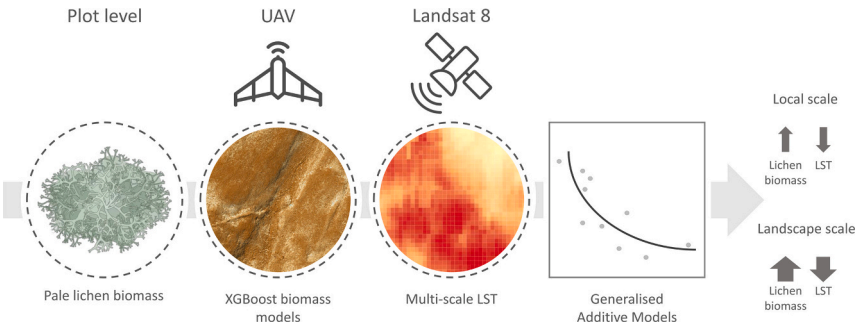

ARTICLE INFO

Editor: Paulo Pereira

Keywords:
Cladonia
Pale lichens
UAV
Landsat

ABSTRACT

Pale terricolous lichens are a vital component of Arctic ecosystems, significantly contributing to carbon balance, energy regulation, and serving as a primary food source for reindeer. Their characteristically high albedo also impacts land surface temperature (LST) dynamics across various spatial scales. However, remote sensing of lichens is challenging due to their complex spectral signatures and large spatial variations in coverage and biomass even within local landscape scales. This study evaluates the influence of pale lichens on LST at local and landscape scales by integrating RGB, multispectral, and thermal infrared imagery from an Unmanned Aerial Vehicle

* Corresponding author at: Department of Geographical and Historical studies, University of Eastern Finland, P.O. Box 111, FI-80101 Joensuu, Finland.
E-mail address: miguel.villoslada@uef.fi (M. Villoslada).
[1] These authors contributed equally to this work and share first authorship.

https://doi.org/10.1016/j.scitotenv.2025.178982
Received 16 September 2024; Received in revised form 24 February 2025; Accepted 24 February 2025
Available online 1 March 2025

Tundra
Temperature
Satellite
Arctic

(UAV) with multi-temporal Landsat 8 thermal data. An Extreme Gradient Boosting algorithm was employed to map pale lichen biomass, areal extent, and the occurrence of major plant functional types in the sub-arctic heath tundra landscape in the Jávrrešduottar and Sieiddečearru areas on the Finland-Norway border. Generalized Additive Models (GAMs) were used to elucidate the factors affecting LST. The UAV model accurately predicted pale lichen biomass (R^2 0.63) and vascular vegetation cover (R^2 0.70). GAMs revealed that pale lichens significantly influence thermal regimes, with increased biomass leading to decreased LST, an effect more pronounced at the landscape scale (deviance explained 47.26 % and 65.8 % for local and landscape models, respectively). Pale lichen biomass was identified as the second most important variable affecting LST at both scales, with elevation being the most important variable. This research demonstrates the capability of UAV-derived models to capture the heterogeneous and fine-scale structure of tundra ecosystems. Furthermore, it underscores the effectiveness of combining high spatial resolution UAV and high temporal resolution satellite platforms. Finally, this study highlights the pivotal role of pale lichens in Arctic thermal dynamics and showcases how advanced remote sensing techniques can be used for ecological monitoring and management.

1. Introduction

Lichens cover around 8 % of the Earth's land surface (Crittenden, 2000; Elbert et al., 2012). While possessing the ability to colonize almost all terrestrial habitats, they play a key role in various ecosystem functions particularly at high altitudes and latitudes (Asplund and Wardle, 2017). Driven by morphological and biochemical adaptations (Sonesson and Callaghan, 1991; Cornelissen et al., 2007), lichens exhibit a high tolerance to cold temperatures and drought (Pannewitz et al., 2003; Bjerke et al., 2011), which allows them to act as pioneers and establish and grow in habitats with extreme conditions (Armstrong, 2017).

While lichens can vary in color, pale lichens are believed to play an important role in regulating energy and carbon balance in high-latitude ecosystems (Bjerke et al., 2024), since they control soil temperature regimes through the reflection of shortwave radiation (Soudzilovskaia et al., 2013; Aartsma et al., 2020). Pale fruticose ground lichens are known for their high albedo (Beringer et al., 2005) and their influence on broadband shortwave reflectance has been thoroughly researched at various spatial scales, from plot (Finne et al., 2023) to landscape (Cohen et al., 2013). Due to their reflectance properties, changes in lichen cover and biomass may result in shifts in surface and soil temperature regimes, potentially affecting the release of carbon from the soil to the atmosphere (Schuur et al., 2007), and triggering changes in the ecosystem composition (Elmendorf et al., 2012; Fraser et al., 2014). *Cladonia* sp. lichens also constitute a key component of reindeer (*Rangifer tarandus*) diet in Fennoscandian reindeer herding areas (Tømmervik et al., 2012), consequently being subject to the effects of grazing, trampling, and changes in reindeer management regimes (Kumpula, 2006; Akujärvi et al., 2014; Cohen et al., 2013). Reindeer grazing on pale lichens could therefore trigger shifts in surface albedo in tundra-like environments (Bjerke et al., 2024).

However, LST dynamics and lichen volumes can show sharp variations across space, and the linkages between ecosystem structure and LST may vary depending on the spatial scale of assessment. For instance, Yang et al. (2021) showed how fine scale composition of plant functional types accounted for a large share of the variation in thermoregulation at the landscape scale. To study the influence of pale lichens on surface temperatures adequately, spatially explicit tools able to address multiple spatial scales are needed. In this regard, the emergence of machine learning algorithms in combination with remote sensing has provided the means to model changes in pale lichen cover (Kennedy et al., 2020; He et al., 2024) and biomass (Erlandsson et al., 2022). Although these studies provide accurate results of temporal changes in lichen cover and biomass, the coarse spatial resolution of satellite imagery may conceal both the effects of pale lichens on thermal dynamics, and the reindeer herbivory effects on pale lichen cover and biomass, since both phenomena occur at highly local spatial scales. To counteract the coarse grain size of satellites, recent studies have taken advantage of the very high-resolution images provided by Unoccupied Aerial Vehicles (UAVs) to map the extent of lichen species (Fraser et al., 2022; Richardson et al., 2021; He et al., 2024).

However, despite the recent advances in UAV-based remote sensing techniques and the multiple studies addressing pale lichen effects on albedo, there are still several subjects requiring a deeper understanding. Most studies utilizing UAVs have focused on estimating lichen cover. As Erlandsson et al. (2022) have pointed out, lichen volume or biomass are more relevant ecological measures, showing a closer relation with albedo and vegetation dynamics in tundra environments. In this regard, a significant research gap exists concerning the capability and potential limitations of very high-resolution UAV imagery for mapping lichen biomass. This gap is particularly relevant given the unique spectral behaviour and physiological characteristics of lichens (Nelson et al., 2022). Additionally, it remains unclear whether lichen biomass, rather than the more commonly studied lichen cover, has a measurable impact on land surface temperature (LST). Most critically, there is a lack of studies explicitly exploring the relationship between pale lichen biomass and LST across multiple spatial scales. Resolving this gap could enhance our understanding of scale-dependent effects. We address these knowledge gaps, specifically asking:

- Whether UAV-derived imagery can be used to map and model pale lichen biomass.
- Whether pale lichen biomass within pale lichen-dominated areas have an effect on land surface temperature.
- What is the magnitude of the differences in land surface temperature between areas dominated by pale lichens and those dominated by vascular vegetation
- How the relationship between land surface temperature, pale lichen biomass, and other environmental variables varies between local and landscape spatial scales (UAV-based vs satellite-based LST).

2. Materials and methods

2.1. Study sites

We carried out the study on the border between Norway and Finland, in the Jávrrešduottar and Sieiddečearru areas, within the Enontekiö (FIN) and Kautokeino (NOR) municipalities (Fig. 1). The topography of the region is undulating, and the sites are situated at an elevation ranging from 250 to 620 m above sea level. In Enontekiö, the average winter (December to February) and summer (June to August) temperatures were − 11.3 °C and 9.5 °C, respectively, and the average winter and summer precipitation 139 and 188 mm, respectively, during 1991–2020, with snow cover typically lasting from late October to late May (Finnish Meteorological Institute, 2024).

The study areas are typical sub-Arctic treeless fell tundra heaths and populated by ericaceous shrubs, *Betula nana,* and *Cladonia* lichens (Kumpula, 2006). Depressions within the landscape feature fens ranging

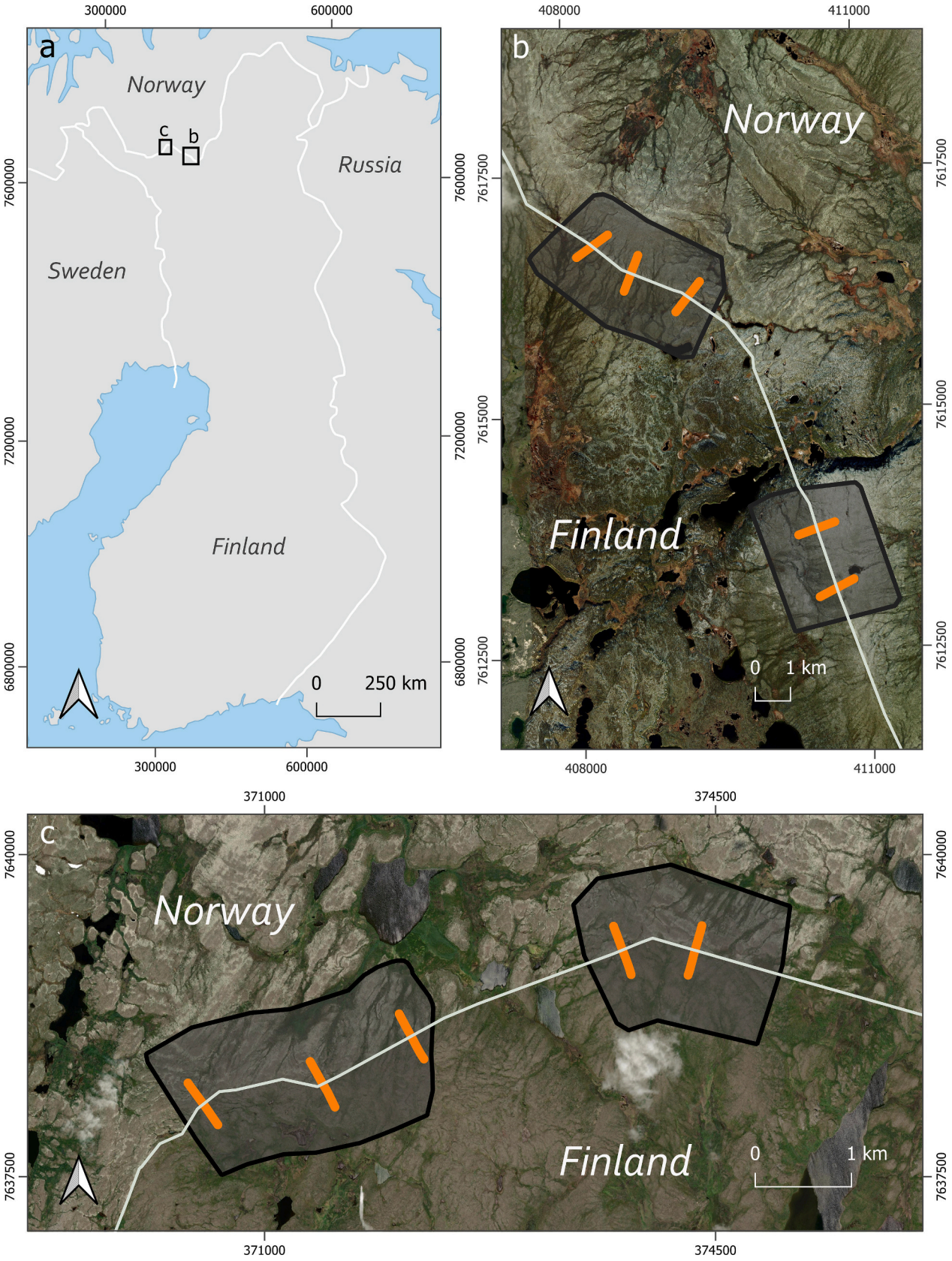

Fig. 1. Panel *a* shows the location of the study sites in northern Fennoscandia, between Norway and Finland, while panels *b* and *c* present a close-up view of Sieiddečearru and Jávrrešduottar respectively. The orange lines denote the vegetation sampling transects, the white line indicates the grazing fence, and the dark polygons correspond to the areas surveyed with a UAV. Source of background imagery: *ESRI satellite*. (Proj: ETRS-TM35FIN).

from poor to moderately rich nutrient status (with soils classified as WRB Dystric Histosols according to the Finnish Soil Database[2]), characterised by sedges such as *Carex rostrata*, *Carex rotundata*, and *Eriophorum angustifolium*, along with bryophytes like *Sphagnum riparium*, *S. lindbergii*, *S. teres*, *Paludella squarrosa*, and *Sarmentypnum sarmentosum* (Kolari et al., 2019).

We selected the two study sites based on the strong contrasts in pale lichen coverage and biomass. In the mid-1950s, a fence was built following the border between Finland and Norway, to prevent reindeer crossing from one country to another. The Norwegian side of the fence is used as winter grazing grounds when reindeer mainly feed on *Cladonia* spp. lichens buried under the snow. In contrast, the areas on the Finnish side of the border have been used as spring and summer pastures since the 1930s (Villoslada et al., 2023), where lichen heaths have been subjected to long-term trampling and grazing during periods without snow. Over the years, this has led to stark differences in pale lichen coverage and volume across the grazing fence (Erlandsson et al., 2022), with higher lichen cover and biomass in the Norwegian side.

2.2. Overview of methods

Our methods were divided into 3 main steps: (1) Retrieval of in-situ and remote sensing data, (2) Pale lichen biomass and vegetation modelling, and (3) Unveiling the effects of pale lichens on LST (Fig. 2). We modeled pale lichen biomass and vascular plants cover utilizing various co-predictors derived from UAV images and a machine learning model, in combination with plot-level data. We further used Generalized Additive Models (GAMs) to reveal the effects of pale lichens along with topographic metrics and vascular vegetation on land surface temperature (LST) at two contrasting spatial scales. At the local scale, we retrieved LST from a UAV-mounted thermal sensor. At the landscape scale, we obtained multitemporal LST readings from the Landsat 8 Operational Land Imager.

2.3. Data collection

We conducted vegetation surveys in the Jávrrešduottar area in July 2020 and in the Sieiddečearru area in July 2021 (Fig. 1). At both sites, we established 5 transects with a length of 400 m each, laid perpendicularly across the border fence, resulting in 200 m on each side. Along the transects, we positioned a total of 400 vegetation plots (0.5 × 0.5 m) at 10-m intervals. We recorded the location of each vegetation plot using an RTK GNSS (Topcon Hiper V). We conducted a comprehensive assessment of the vegetation within each plot, encompassing the visual estimation of %-coverage for all vascular plants, bryophytes, and lichen species present. We measured the average height of each vascular plant and lichen species using a ruler. The recorded lichen cover data were used to estimate the volumetric representations of pale lichens within the study plots, utilizing the following formula:

$$w = 22 \times c \times h \quad (1)$$

where *w* is lichen dry weight biomass g m^{-2}, *c* demotes lichen coverage as a percentage, *h* represents the mean lichen height in millimeters, and 22 is a regression coefficient between weight and volume estimated in controlled lab conditions (Gaare and Tømmervik, 2000; Tømmervik et al., 2012).

We considered the following pale lichens: *Cladonia arbuscula/mitis*, *Cladonia rangiferina*, *Cladonia stellaris*, *Cladonia stygia*, *Cladonia uncialis*, *Flavocetraria nivalis*, *Flavocetraria cucullata*, *Stereocaulon alpinum/paschale*, and *Thamnolia vermicularis*. From *Cladonia* lichens, we included the species without basal squamules and with (richly) branched or spiky podetia, without cups (Hodgetts, 1992). Other *Cladonia* species, such as *C. crispata* and *C. gracilis*, occur in the study region as well but with low cover and volume compared to the abundance of the other species. When selecting pale lichens, we considered the color, structure, and abundance of species. First, we selected mat-forming lichen species that are white or pale (Erlandsson et al., 2022). Although we also identified all miniature cup-forming or "needle-like" Cladonia species, these were later excluded from analysis due their wide range of colors, from pale to dark brown, and their sparse occurrence (<1 % in the field plots). Further, we grouped vascular plant species in functional and taxonomical plant groups as follows: *Betula nana*, other deciduous shrubs (including primarily *Salix* species and *Vaccinium myrtillus*, evergreen shrubs (including primarily *Empetrum nigrum* and *Calluna vulgaris*), forbs, graminoids, and the family *Lycopodiaceae*.

2.4. UAV data collection and pre-processing

We carried out one UAV survey at each site (mid-July- 2020 and mid-August 2021), encompassing 434 ha at Jávrrešduottar and 358 ha at Sieiddečearru, respectively, utilizing a Sensefly Ebee X fixed wing UAV equipped with a Parrot Sequoia 1.2-megapixel 4-band multispectral sensor (Green [530–570 nm], red [640–680 nm], red edge [730–740 nm], and near-infrared [770–810 nm]) and a SenseFly S.O.D.A RGB camera. Preceding each multispectral flight, we performed a radiometric calibration of the Parrot Sequoia sensor using an Airinov calibration panel. Further, we collected land surface temperature (LST) imagery over a 1000 × 240 m transect across the fence at Jávrrešduottar (Fig. 2) on 29/06/2023 between 12:20 and 13:00 (EEST). For this purpose, we used a DJI Matrice 300 RTK equipped with a Micasense Altum-PT camera, which incorporates a built-in radiometrically calibrated FLIR LWIR Boson thermal sensor with a thermal sensitivity of 0.05 °C. The spatial resolution of the remotely sensed data was 16, 10, and 3.5 cm per pixel for the thermal (Altum-PT), multispectral (Parrot Sequoia), and RGB (S.O.D.A. RGB) images respectively. All flights were undertaken in sunny conditions and with windspeeds under 7 m/s. Both the fixed-wing and quadcopter flights were set in follow terrain mode, flight altitudes of 120 m for Ebee X, and 60 m for Matrice 300, and front and side overlaps of 75 % and 70 % for Ebee X, and 70 and 75 for Matrice 300. The thermal survey required two flights, while the multispectral and RGB required 5 flights per sensor at Jávrrešduottar and 4 at Sieiddečearru.

We processed UAV imagery sets in eMotion 3®, utilizing a post-process kinematic correction to ensure accurate geolocation of the images. We employed RINEX observation and navigation files sourced from the FinnRef CORS network to enhance positional accuracy (Zhang et al., 2019a, 2019b). Subsequently, we generated RGB, multispectral, and thermal orthomosaics using Pix4D v.4.3.31®, resulting in one RGB and two spectral orthomosaics for each research site. To assess the UAV-derived LST imagery, we measured surface temperature using a handheld infrared thermometer gun in 20 randomly selected points located with an RTK-GNSS device, and compared both readings using a pearson's r (considering correlations statistically significant at $p < 0.05$).

2.5. Pale lichen biomass and vegetation fractional cover models

2.5.1. Co-predictors set

The co-predictor set used in the machine learning models consisted of a combination of multispectral (derived from the Parrot Sequoia 1.2-megapixel sensor) and topographic spatially continuous raster layers (derived from the S.O.D.A. RGB sensor). We computed a set of 17 vegetation indices (VIs) (Table 1) using the spectral band raster layers. Among these, we included the biological soil crust index (BSCI), which has been specifically created to map lichen-dominated soil crusts (Chen et al., 2005). We selected the remaining VIs based on their ability to disentangle spectral signatures associated with differences in pigmentation, AGB, water content, leaf area, or soil reflectance (Villoslada

[2] https://paituli.csc.fi/download.html?data_id=luke_soildb_250k_2016_shp_euref, accessed on 21/02/2025

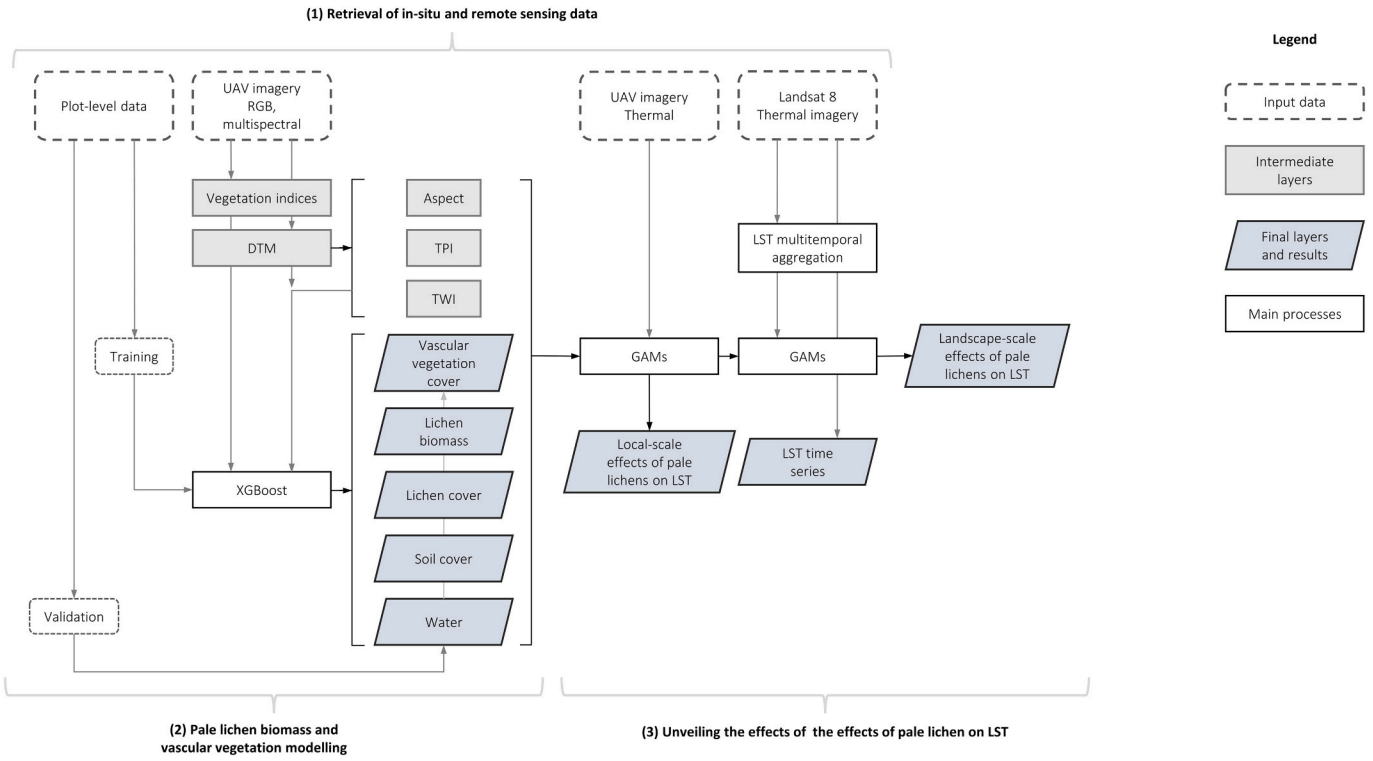

Fig. 2. Summarized workflow representing the main steps in this study. DTM: Digital terrain model, GAMs: Generalized additive models, LST: Land surface temperature, TPI: Topographic position index, TWI: Topographic wetness index, UAV: Unmanned aerial vehicle.

et al., 2023).

Topography has been previously linked to the abundance and productivity of lichen species (Bruun et al., 2006). To account for the local variations in topography and their potential effect on pale lichen biomass, we first derived a set of digital terrain models (DTMs) from the UAV data. We used Structure-from-Motion (SfM) in combination with Multi-View stereo photogrammetry to reconstruct 3D point clouds from the UAV-derived RGB images in Pix4Dmapper v.4.3.31® (Smith et al., 2016). We then used a Cloth Simulation Algorithm (Zhang et al., 2016) in CloudCompare (Cloud Compare 2.12.4, 2024) to identify and filter out 3D points corresponding to prominent vegetation such as *Betula nana* and ericaceous shrubs. We set the Cloth Simulation Algorithm parameters as follows: cloth resolution 0.1 m, classification threshold 0.1 m, and terrain set to slope. Once filtered, we used the 3D point cloud to generate DTMs, for which we set a spatial resolution of 10 cm per pixel, matching that of the multispectral images. Using these as a basis, we computed four commonly used topographic indices: Slope, topographic position index (TPI, neighbourhood radius = 20 m), topographic wetness index (TWI), and aspect. Given the large extent of the areas and the size of the datasets, we found the TPI radius of 20 m to be a good compromise between computational efficiency and representativity of the terrain's morphology. For aspect calculations, we first aggregated the 10 cm DTMs to match the size of the units of assessment at the local (5 m diameter hexbins) and landscape scale (30 m Landsat 8 pixels) using the Warp tool with nearest neighbour interpolation in QGIS 3.34. TPI estimates the relative topographic position of a point relative to the mean elevation within a predetermined buffer (Weiss, 2001), while TWI provides an estimation of the effects of topography of hydrological processes by combining upslope contributing area and slope (Sörensen et al., 2006). Here, we used the SAGA wetness index, a variant of the TWI that uses iterative modifications of the catchment area based on the FD8f flow algorithm (Kopecký et al., 2021). We generated the indices in SAGA GIS v 2.3.2. In addition to VIs and topographic indices, we included the four spectral bands (red, green, near-infrared, and red-edge) in the co-predictors dataset. The co-predictor layers were aligned with each other so that raster cells in the dataset overlapped perfectly.

2.5.2. *Extreme gradient boosting model*

We used an Extreme Gradient Boosting algorithm (XGBoost) to model pale lichen biomass and cover, as well as fractional cover of bare soil and functional and taxonomical plant groups (all vascular plants, *Betula nana,* other deciduous shrubs, evergreen shrubs, forbs, graminoids, and the family *Lycopodiaceae*). XGBoost can make predictions beyond the limits of the training dataset when dealing with continuous variables. In addition, XGBoost is known for its robustness to class imbalance and noise, and its ability to handle multicollinearity in the co-predictors set (Man et al., 2018; Zhang et al., 2019b). We used the information collected within the field plots as training data, following a random 50/50 split-sample approach, where 50 % of the plots were devoted to model training, and 50 % to validation of modelling results. We averaged the value of all pixels from each co-predictor layer (spectral bands, VIs, and topographic indices) falling within each sampling polygon, and assigned the corresponding pale lichen biomass, pale lichen fractional cover, bare soil fractional cover, total vascular vegetation %-cover, and plant functional and taxonomical group fractional cover values. To avoid potential biases and noise associated with single model runs, we iterated each model 50 times, with a new random training/validation split in each model iteration. We calculated the result maps as the mean of the 50 iterations results. Additionally, we modeled the distribution of water bodies following a binary classification implemented using an XGBoost algorithm. We manually digitized the training/validation dataset, visually identifying water bodies in the UAV-derived RGB images. For consistency, we digitized 50"water" and 50 "no water" polygons of the same size as the vegetation plots. This process resulted in a binary water mask raster layer. We validated the results of all models using root mean squared error (RMSE), range-normalized root mean squared error (nRMSE), mean absolute error (MAE), bias, and percentage of variance explained by the model (R^2). Finally, we assessed co-predictor importance using the *Gain* metric

Table 1
List of vegetation Indices selected in the present study to predict lichen biomass and vascular vegetation fractional cover. G: Green, GNIR = (G + R + NIR)/3, NIR: Near Infrared, R: Red.

Vegetation and textural index	Equation	Reference
Biological Soil Crust Index (BSCI)	[1–2*abs(R-G)] /GRNIR*	Fang et al. (2015)
Red edge chlorophyll index (CIre)	(NIR/Rededge) – 1	Gitelson et al. (2005)
Chlorophyll vegetation index (CVI)	(NIR/G) × (R/G)	Vincini et al. (2007)
Datt4	R/G*Rededge	Datt (1998)
Difference Vegetation Index (DVI)	NIR-αR α = 0.96916	Richardson and Everitt (1992), Maguigan et al. (2016)
2-band Enhanced Vegetation Index (EVI2)	2.5[(NIR-R)/(NIR + 2.4R + 1)]	Jiang et al. (2008), Jin and Eklundh (2014)
Green Difference Index (GDI)	NIR-R + G	Gianelle and Vescovo (2007)
Green Normalized Difference Vegetation Index (GNDVI)	(NIR-G)/(NIR + G)	Gitelson et al. (1996), Naidoo et al. (2019)
Green-Red Difference Index (GRDI)	(G-R)/(G + R)	Gianelle and Vescovo (2007)
Green Ratio Vegetation Index (GRVI)	NIR/G	Sripada et al. (2006), Naidoo et al. (2019)
Modified Soil Adjusted Vegetation Index (MSAVI)	$0.5*\left[2*NIR - \sqrt{(2*NIR+1)^2} - 8*(NIR-R)\right]$	Qi et al. (1994), Jin and Eklundh (2014)
Normalized Difference Vegetation Index (NDVI)	(NIR-R)/(NIR + R)	Rouse et al. (1974)
Red edge normalized Difference Vegetation Index (NDVIre)	(NIR-Rededge)/(NIR + Rededge)	Gitelson and Merzlyak (1994), Kross et al. (2015)
Normalized Difference Water Index (NDWI)	(G-NIR)/(G + NIR)	He et al. (2021)
Red edge triangular vegetation index (core only) (RTVIcore)	100(NIR-Rededge)-10(NIR-G)	Kross et al. (2015), Clausen et al. (2013)
Soil Adjusted Vegetation Index (SAVI)	[(NIR-R)/(NIR + R + L)](1 + L) L (soil adjustment factor) = 0.5	Huete (1988), Ullah et al. (2012)
Red edge simple ratio (SRre)	NIR/Rededge	Gitelson and Merzlyak (1994), Kross et al. (2015), Naidoo et al. (2019)

within XGBoost (Chen et al., 2019).

2.6. Landsat 8 land surface temperature

To address the landscape scale in the study, we compiled LST imagery corresponding to the entire Landsat 8 collection, i.e., from 2013 to 2023. We undertook a temporal aggregation to avoid potential artifacts and smooth out the effects of single-date or single-year LST readings. We restricted the Landsat-derived LST data to a 10-year window to ensure the representativity of the pale lichen biomass estimates based on field data from 2020 and 2021. Previous studies (Erlandsson et al., 2022) have shown drastic shifts in lichen volume in our study area over several decades, whereas Den Herder et al. (2003) found no significant differences in *Cladonia* spp. biomass within a 13-year period in a heathland in Finnish Lapland. We selected Landsat 8 scenes overlapping the study sites in the months of July and August, therefore avoiding late snowmelt areas (Kivinen et al., 2012) and their potential influence on LST retrieval.

We retrieved LST values at a spatial resolution of 30 m using the methodology developed by Ermida et al. (2020) in Google Earth Engine (Gorelick et al., 2017). The authors used a Statistical Mono-Window (SMW) algorithm to compute LST as a linear function of prescribed surface emissivity and Landsat-observed top of the atmosphere brightness temperature. The prescribed values of surface emissivity were obtained from the ASTER GEDv3 dataset (Malakar et al., 2018) and a vegetation adjustment using Landsat-derived NDVI. The original Landsat 8 at-sensor brightness temperature data (Band 10, 10.6–11.2 μm) are originally recorded at a spatial resolution of 100 m per pixel and resampled by the USGS to 30 m per pixel using the cubic convolution method during Level-1 product generation (Xue et al., 2020). We employed Total Column Water Vapor (TCWV) values from NCEP/NCAR reanalysis data (Kalnay et al., 2018) to resolve the atmospheric effects on the Landsat thermal infrared observations.

Finally, we preselected images based on their cloud cover information, retrieved from the BQA quality assessment band, setting a threshold of 30 %. We visually inspected each of the preselected Landsat 8 LST scenes to ensure that the study sites were not affected by gaps, haze, or cloud shadows. The final list of L8 LST scenes can be found in the supplementary materials (table S.1).

To aggregate and combine L8 LST data with the UAV-derived pale lichen biomass estimates, we transformed the L8 images into vector grids, where individual polygons aligned with the corresponding raster image pixels. We calculated the total July–August average LST during 2013 and 2023 within each polygon, as well as the average LST in July and August each year. To compare the UAV-derived LST measurements with a baseline, we computed the average of the UAV LST readings within the extent of each L8 pixel and correlated this with the 10-year summer LST average obtained from L8. To better visualize potential differences between single-date UAV and multi-date L8 LST, we created a map depicting the departure from the 10-year average, computed as the difference between the UAV and the L8 readings. The results of this step are presented in the supplementary materials (fig. S.3).

2.7. Effects of pale lichen biomass and fractional cover on land surface temperature at the local and landscape scales

We analysed the effects of pale lichen biomass alongside other covariates on LST at two different spatial scales, hereinafter referred to as local scale and landscape scale. The aim of this multi-scale analysis is to explore whether the intensity of the relationship between pale lichen biomass and LST varies across spatial scales, and whether the relative importance of other biophysical factors influencing this relationship show scale-specific patterns. We built the local scale analysis upon the UAV-derived LST data collected at the transect site and a number of biophysical co-predictor layers overlapping the transect. To avoid pixel-level noise and ensure a balance between capturing the fine-grain

characteristics of the landscape and maintaining a sufficient amount of data for subsequent GAM analyses, we aggregated LST, pale lichen biomass, and all additional UAV-derived variables into maps composed of hexagonal bins (hexbin) with a diameter of 5 m. While the hexbin size is somewhat arbitrary, it represents a practical compromise that achieves this balance (Villoslada et al., 2023). Within each hexbin, we calculated the average value of each variable. Further, we undertook a regional scale analysis using the total July–August average L8 LST. To match the spatial scales of L8-derived LST and UAV-derived pale lichen biomass, we calculated the average of pale lichen biomass and other UAV-derived variables within each of the L8 vector grid polygons.

Prior to the analysis, we undertook a multicriteria filtering approach to disentangle the multiple and complex factors potentially affecting LST in tundra landscapes. Firstly, we narrowed down the areas under analysis using a TPI-based landform classification in SAGA GIS. The algorithm uses the topographic position index to derive a set of 10 landforms (Fig. S.1 in supplementary materials). To rule out the potential effects of soil moisture gradients on LST, we focused the assessment on the landforms classified as plains, open slopes, and upper slopes, which are also the dominant landforms in the study area, covering 76 % of the studied landscape. This way, we discarded landforms such as streams, drainages, and valleys, associated to higher soil moisture levels and very low occurrence of lichens. We further refined our analysis by defining threshold for fractional vascular vegetation cover, selecting areas with a vascular vegetation cover below 50 %. By doing so, we partially avoid the effects of evapotranspiration, stomatal conductance, or canopy complexity (Gersony et al., 2016) or on LST associated to densely vegetated areas.

We assessed the relationship between pale lichen biomass and land surface temperature using generalized additive models (GAMs) due to their ability to handle complex and nonlinear relationships (Simpson, 2018; Viana et al., 2022). We constructed the GAMs utilizing the *mgcv* package (Wood and Wood, 2015), with restricted maximum likelihood (REML) and a gaussian distribution. Smooth parameters were set to 4 degrees of freedom (k = 4), which allows to unveil non-linear relationships while avoiding overfitting. In addition to pale lichen biomass, we included eight other explanatory variables that have shown strong linkages with LST in previous studies: pale lichen fractional cover, vascular plant vegetation fractional cover, aspect, topographic position index, topographic wetness index, soil fractional cover, distance to water (calculated in QGIS 3.34 as the Euclidean distance between all pixels and pixels classified as water in the previous step), and elevation. For instance, Hope et al. (2005) linked increases in vegetation fractional cover and NDVI with increases in LST. Likewise, elevation and aspect (He et al., 2019a, 2019b, Nill et al., 2019), soil moisture (Nill et al., 2019), bare soil and water (Muster et al., 2015), and topographic position (Van De Kerchove et al., 2013) have shown strong relationships with LST in tundra and mountainous environments. This wider set of explanatory variables aims at addressing the complexity of land surface temperature dynamics, as well as to frame the relative contributions of pale lichen biomass to land surface temperature. We ran a variance inflation factor (VIF) analysis to detect multicollinearity and discard highly correlated variables, considering a VIF value higher than 10 as a strong indicator of multicollinearity (Zhao et al., 2014, Kanaji et al., 2017, He et al., 2019a, 2019b). We used to vif.gam function in the R package mgcv.helper[3] to run the VIF tests. To select the model with the highest explanatory power while minimizing the effect of irrelevant and redundant explanatory variables, we ran all possible additive combinations of variables (Barboza et al., 2019; Quillfeldt et al., 2022) using the function dredge in the R package MuMIn (Barton and Barton, 2015). The dredge function ranks models based on their ability to minimize the Akaike information criterion (AIC). We ran the dredge variable selection on the full models for UAV and Landsat 8 LST.

[3] (https://github.com/samclifford/mgcv.helper, accessed on 07/05/2024)

To assess the importance of each explanatory variables in the GAMs, we used two different yet complementary metrics: Relative importance (RI) and partial deviance explained (D^2). Both metrics were computed for the selected local and landscape scale models. To estimate the RI of each explanatory variable, we applied the sum of AICc weights (AICcw) method (Barboza et al., 2019). The dredge function ranks candidate models based on the Akaike information criterion for small sample sizes (AICc) and computes differences in AICc (ΔAICc) and AICc weights (AICcw) for each model. AICcw represent the likelihood that a given model is the best among the set of fitted models (Debeffe et al., 2017), given the set of candidate models and the explanatory dataset (Burnham and Anderson, 2002). Following the work developed in previous studies (Barboza et al., 2019; Burnham and Anderson, 2002; Zuur et al., 2009), we computed the RI of each explanatory variable retained in the selected models extracting a list of candidate models with a ΔAICc $\leq$4, and subsequently calculating sum of the AICcw of those models where the variable was included. Thus, the RI (ranging between 0 and 1) represents the likelihood of a particular explanatory variable to be included in the best performing model. We further calculated the partial D^2 of each co-predictor, defined by Lai et al. (2024) as the individual D^2 explained by each predictor from the overall D^2 explained by the model, where all partial D^2 ad up to 100 %. Therefore, partial D^2 represents the relative contribution of each explanatory variable to the overall explanatory power of the model. We calculated the proportion of deviance explained by each predictor using the *gam.hp* package (Lai et al., 2024).

To discriminate potential site-specific conditions at the L8 landscape scale, we ran GAMs for Jávrrešduottar and Sieiddečearru separately. To find whether there are differences in land surface temperature between pale lichen-dominated and vascular vegetation-dominated areas, we used a Welch ANOVA test followed by a Games-Howell pairwise post-hoc test, considering differences statistically significant when $p < 0.05$. Prior to the test, we performed a data filtering process. At the local scale, we defined a 50 % fractional cover threshold for an individual hexbin to be ascribed to one of the vascular plant groups defined in the study, thereby discarding highly heterogeneous hexbins. For a hexbin to be considered dominated by pale lichens, we defined three thresholds: over 50 % pale lichen fractional cover, under 50 % vascular vegetation fractional cover, and average pale lichen biomass over the 3rd quartile of the biomass distribution within the study areas.

At the landscape scale, we compared the average LST between pale lichen-dominated and vascular vegetation-dominated L8 pixels, following the same thresholding criteria as above. At this scale, the highly mixed and patchy nature of tundra heath vegetation prevented us from selecting L8 pixels with a dominant vascular plant group; therefore, we pooled all vascular vegetation into one group. We compared LST values monthly, calculating the average L8 LST corresponding to July and August each year within selected pixels. For each month with available LST data, we undertook pairwise comparisons using a Mann-Whitney *U* test (considering differences statistically significant at $p < 0.05$), given the non-normal distribution of the dataset.

3. Results

3.1. UAV-based lichen and vascular vegetation models

The XGBoost models yielded moderate to high accuracies (Table 2), with the lichen biomass model reaching a R^2 of 0.63 and nRMSE of 0.09. The highest accuracies were achieved in the evergreen shrubs cover model (R^2 0.71, nRMSE 0.11), while the lowest values corresponded to the bare soil cover model with an nRMSE of 0.68. The bias of predictions was low, with response variables being generally slightly underestimated. The maps generated by the XGBoost models (Fig. 3) clearly reflect the contrasting reindeer grazing and trampling patterns across the fence: Both pale lichen fractional cover and biomass show considerably higher values in Norway.

Among all the variables used in the pale lichen biomass predictions,

Table 2
Validation results for the XGBoost models predicting pale lichen biomass, pale lichen fractional cover, soil fractional cover, vascular vegetation fractional cover, and fractional cover of plant functional and taxonomical groups. R^2: Percentage of variance explained by the model; RMSE: root mean squared error; nRMSE: range-normalized root mean squared error; MAE: mean absolute error.

	R^2	RMSE (g m^{-2})	nRMSE	Bias	MAE
Pale lichen biomass	0.63	203.89	0.09	4.76	110.66
Pale lichen cover	0.68	13.70	0.16	0.70	9.36
Vascular vegetation cover	0.70	13.35	0.14	0.22	9.34
Bare soil cover	0.67	13.70	0.68	0.14	9.52
Betula nana cover	0.66	8.50	0.10	−0.02	5.98
Other deciduous species cover	0.65	6.28	0.07	−0.08	3.39
Evergreen shrubs cover	0.71	10.86	0.11	0.35	7.21

topography metrics (aspect, TPI, and slope, Fig. S.2) emerged as the most important, according to the *Gain* metric. Pale lichen percentage cover displayed similar trends, with TPI, red band, and aspect being the most important variables.

3.2. Local scale effects of pale lichen biomass and fractional cover on LST

At the local scale, the VIF analysis did not show multicollinearity between co-predictors (VIF < 10 in all cases). The most parsimonious model included five predictors (lichen biomass, vegetation cover, aspect, TPI, and elevation), explaining 47.26 % of the deviance in land surface temperature (Table 3). The relative importance and the partial D^2 explained by each of the predictors show the relatively larger influence of elevation (RI = 1.00, partial D^2 = 60.35 %) and pale lichen biomass (RI = 1.00, partial D^2 = 21.36 %) on LST in comparison with other covariates. In contrast, TPI and vascular vegetation cover showed relatively lower contributions, with D^2 values of 2.52 % and 4.56 % respectively, and RIs of 0.98 and 0.51 All selected predictors showed significant contributions (pv < 0.05) to the model.

A gradual increase in pale lichen biomass led to a smooth decrease in land surface temperature (Fig. 4.a). On the contrary, elevation (Fig. 4.c) showed a much more complex relationship with land surface temperature, following a sinusoidal correlation. Other variables display weaker relationships with LST (Fig. 4). For instance, increases in the cover of vascular vegetation led to a very slight increase in LST (Fig. 4.b). Additionally, following the expected trend, south facing slopes presented higher LST when compared to other orientations (Fig. 4.e).

LST exhibited marked and significant (pv < 0.05) differences between plant and lichen groups, as revealed by the violin plots (Fig. 5) and the Welch ANOVA and Games-Howell tests (Table S.2 in supplementary materials). The lowest average LST corresponded to areas characterised by a dense pale lichen coverage (avg. LST = 22.79 °C), comparable to that of the *other deciduous* group (22.84 °C). Areas covered by species corresponding to the evergreen species presented the highest LST value (33.81 °C) significantly higher than the average LST associated to *Betula nana* (26.33 °C) and *other deciduous* species.

3.3. Landscape scale effects of pale lichen biomass and fractional cover on LST

In addition, there was a marked difference in the time-aggregated LST between study sites, with Sieiddečearru displaying generally

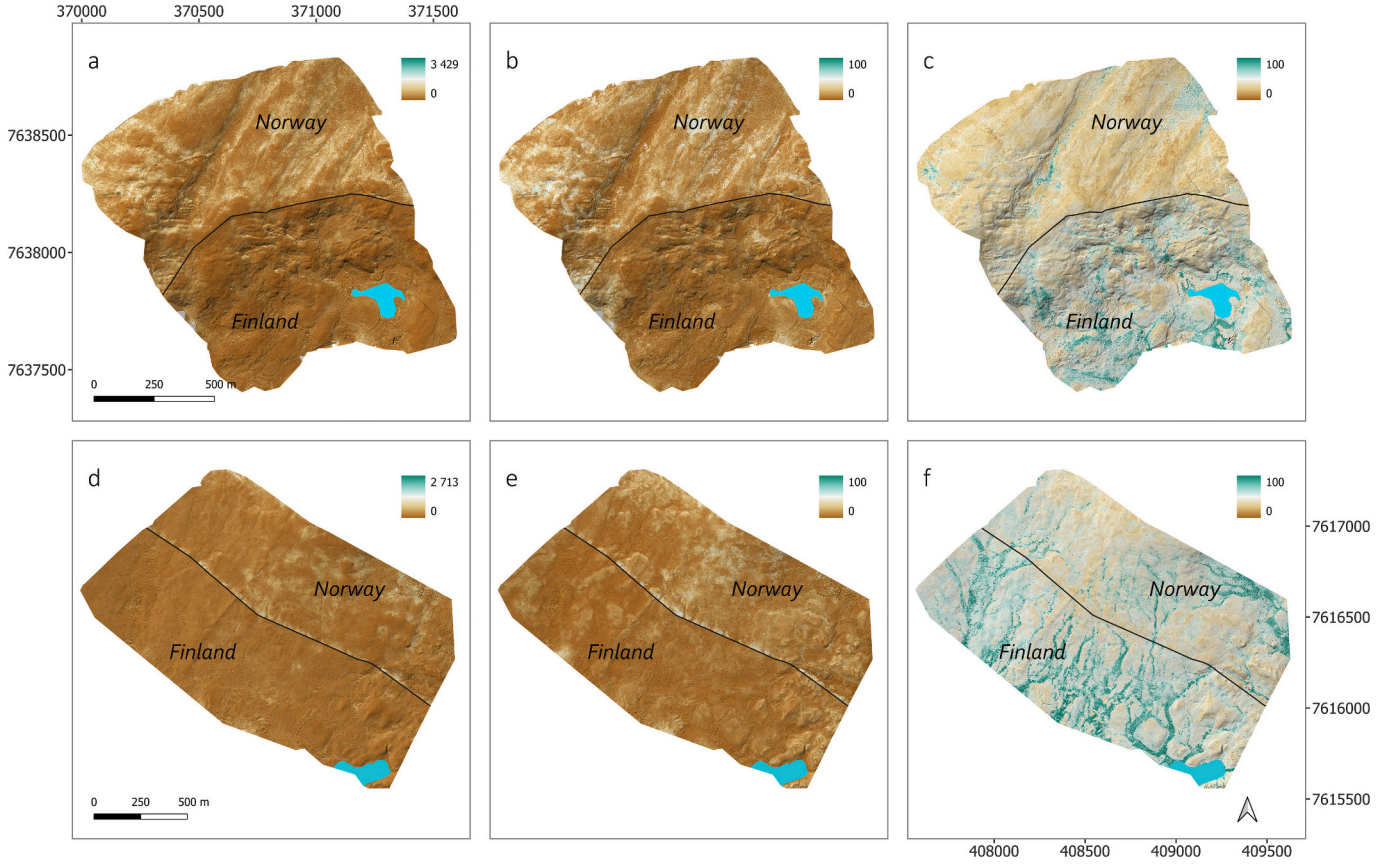

Fig. 3. XGBoost model predictions for pale lichen biomass (a,d), pale lichen fractional cover (b, e), and total vascular vegetation fractional cover (c,f). The maps represent sections of the study sites *Sieiddečearru* (a, b, and c) and *Jávrrešduottar* (d, s, and f), overlaid on top of a shaded relief map. Pale lichen biomass is expressed as gr m^{-2} and pale lichen and vascular vegetation cover as percentage cover within a pixel. The dark grey line denotes the grazing fence between Finland and Norway.

Table 3
Results of GAMs assessing the effect of nine smooth terms on UAV-derived LST for the transect site. The model summary includes the total percentage of deviance explained (D^2), the F statistic, the relative importance of each smooth term (RI), and the partial deviance explained by each predictor (partial D^2). Predictors are shown as GAM smooth terms. TPI: Topographic Position Index. Significant contributions of smooth terms are highlighted with asterisks, where * indicates significant contribution at the 0.05 level, ** indicates significant contribution at the 0.01 level, *** indicates significant contribution at the 0.001 level, and **** indicates significant contribution at the 0.0001 level. ns: not significant.

Smooth terms	F value*	pv	Relative importance	Partial D^2 (%)
s(lichen biomass)	27.17	****	1.00	21.36
s(vegetation cover)	2.45	***	0.51	4.56
s(aspect)	6.33	***	0.84	11.20
s(tpi)	2.93	****	0.98	2.52
s(elevation)	17.91	****	1.00	60.35
Overall deviance explained	**47.26**%			

*The F value evaluates the significance of each smooth term in the model, calculated as the ratio of the mean square of the model to the mean square of the residuals.

lower temperatures than Jávrrešduottar at the same time period (Fig. 6. a). The comparison between the single-date UAV and the 10 years average L8 LST data yielded a strong correlation (pearson's $r = 0.84$, $p < 0.001$, RMSE = 2.83 °C) (Fig. S.3) even though the differences in spatial resolution between L8 and UAV were clearly observable in the maps (Fig. 6). The comparison map further revealed a small departure of the UAV LST readings from the 10 years average, with difference values ranging between −3.46 °C and 6.81 °C (Fig. S.3).

The VIF analysis at the landscape level revealed multicollinearity between pale lichen biomass and cover at Jávrrešduottar, and therefore only biomass was included in the model computations. The landscape-scale GAMs analysis combining UAV and Landsat 8 datasets revealed distinct patterns at the study sites. The most parsimonious model in Jávrrešduottar included 5 co-predictors (lichen biomass, vegetation cover, aspect, bare soil cover, and elevation), presenting an overall D^2 of 65.8 % (Table 4), therefore entailing a higher explanatory power than the local-scale UAV-based model (Table 3). Similarly, the partial D^2 and RI corresponding to each of the smooth terms was generally higher than that of the UAV-based model, with elevation and pale lichen biomass standing out as the most important smooth terms (RI and partial D^2 values of 1.00 and 55.21 % for elevation, and 1.00 and 32.55 % for lichen biomass respectively). On the contrary, the Sieiddečearru model underperformed when comparing the total and partial D^2 values to the Jávrrešduottar Landsat 8 and the UAV models (overall $D^2 = 26.50$ %). In this model, it is worth mentioning the role of aspect in explaining the variability of LST within the Jávrrešduottar study site (RI = 0.99, partial $D^2 = 54.70$ %), as well as the meagre contribution of pale lichen biomass (RI = 0.54, partial $D^2 = 4.68$).

The GAM plots for Jávrrešduottar (Fig. 7) confirm that models based on the combination of aggregated L8 time series and UAV data present stronger trends than those based on single-time UAV data only. The effect of pale lichen biomass on the average summer LST (RI = 1.00, partial $D^2 = 32.55$ %, Fig. 7 a) showcases a potential saturation effect, where the initially negative correlation gradually flattens as biomass increases. The effect of vascular vegetation on LST (Fig. 7.b) in lichen-dominated areas followed the trend previously observed at the local scale (Fig. 4), with a positive correlation between vascular vegetation fractional cover and LST. The partial contributions of each predictor also revealed a non-linear positive relationship between elevation and LST (RI = 1.00, partial $D^2 = 55.21$, Fig. 7.e), with a flattening trend towards higher elevations.

3.4. LST time series

The mean monthly (July and August) LST between 2013 and 2023 followed a very similar trend in L8 pixels dominated by pale lichens and those dominated by vascular vegetation (Fig. 8). Further, the Mann-Whitney *U* test revealed significant differences in LST between vascular vegetation and lichen-dominated in all months except one (August 2013). L8 pixels dominated by vascular vegetation showed a significantly higher LST than those dominated by pale lichens.

4. Discussion

4.1. UAV-based models of pale lichen cover and biomass

The models we developed achieved moderate to high accuracies, both for pale lichen percentage cover and pale lichen biomass (R^2 values of 0.63 and 0.68, respectively). These results are especially relevant considering the marked spatial heterogeneity of tundra vegetation (Fletcher et al., 2012; Virtanen and Ek, 2014), and the fine spatial-scale effects of reindeer herbivory and trampling on vegetation (Egelkraut et al., 2020). Our centimetre-scale models provide an accurate visual representation of variations in pale lichen coverage and biomass, revealing the differences in lichen biomass across the fence at our study sites (Fig. 3), while simultaneously predicting vascular vegetation composition (Table 2). This is essential to place the potential effects of pale lichen on LST in the right context and account for the effects of vascular vegetation on local thermal regimes. The pale lichen biomass spatial patterns obtained for the study sites aligned well with those presented by Erlandsson et al. (2022) at the same locations, with marked differences in pale lichen across the Finnish-Norway border fence.

The XGBoost variable importance assessment revealed the key role of topography metrics in predicting pale lichen biomass, confirming previous observations that spectral information may not always be sufficient to reflect environmental factors underpinning ecosystem structure (Martínez Prentice et al., 2021; Erlandsson et al., 2022; Villoslada et al., 2022). Specifically in the case of pale lichen biomass models, the three most important co-predictors were aspect, TPI, and slope. In tundra landscapes, these three variables have been linked to moisture regimes and snow depth (Bennett et al., 2021; Meloche et al., 2022), which in turn, play a crucial role in the development of lichen mats (Inoue et al., 2017; Barták et al., 2021). Local topography is also tightly linked to reindeer grazing patterns in wintertime, when reindeer dig craters through the snow to access lichens (Ims Vistnes and Nellemann, 2008). Exposed ridges with shallow snow cover offer easier digging grounds, as opposed to local depressions and snow accumulation areas, or areas characterised by hardened snow and ice layers, which may be avoided by reindeer (Helle, 1984; Kumpula and Colpaert, 2007).

5. Effects of pale lichen biomass on land surface temperature at multiple scales

The GAMs captured the effect of pale lichen biomass on LST, with larger biomass leading to decreased LST values (Tables 3 and 4). However, the magnitude of this effect appeared to be dependent on the spatial and temporal scales of analysis, with a much higher percentage of variance explained by the L8-based model (overall $D^2 = 65.8$ %, pale lichen biomass partial $D^2 = 32.55$ % at Jávrrešduottar) than the UAV-based model (overall $D^2 = 47.26$ %, pale lichen biomass partial $D^2 = 21.36$ % at the transect site). Regarding the spatial scale of assessment, it has been previously elucidated that the aggregation of information associated to large-size pixels leads to a decrease in the heterogeneity of the data captured, but a higher degree of model fit (Mao et al., 2022; Räsänen and Virtanen, 2019). In addition to this, local-scale factors such as wind, eddies, moisture, and cloud shading may be partially overriding the effect of pale lichen biomass and other UAV-derived co-predictors on LST.

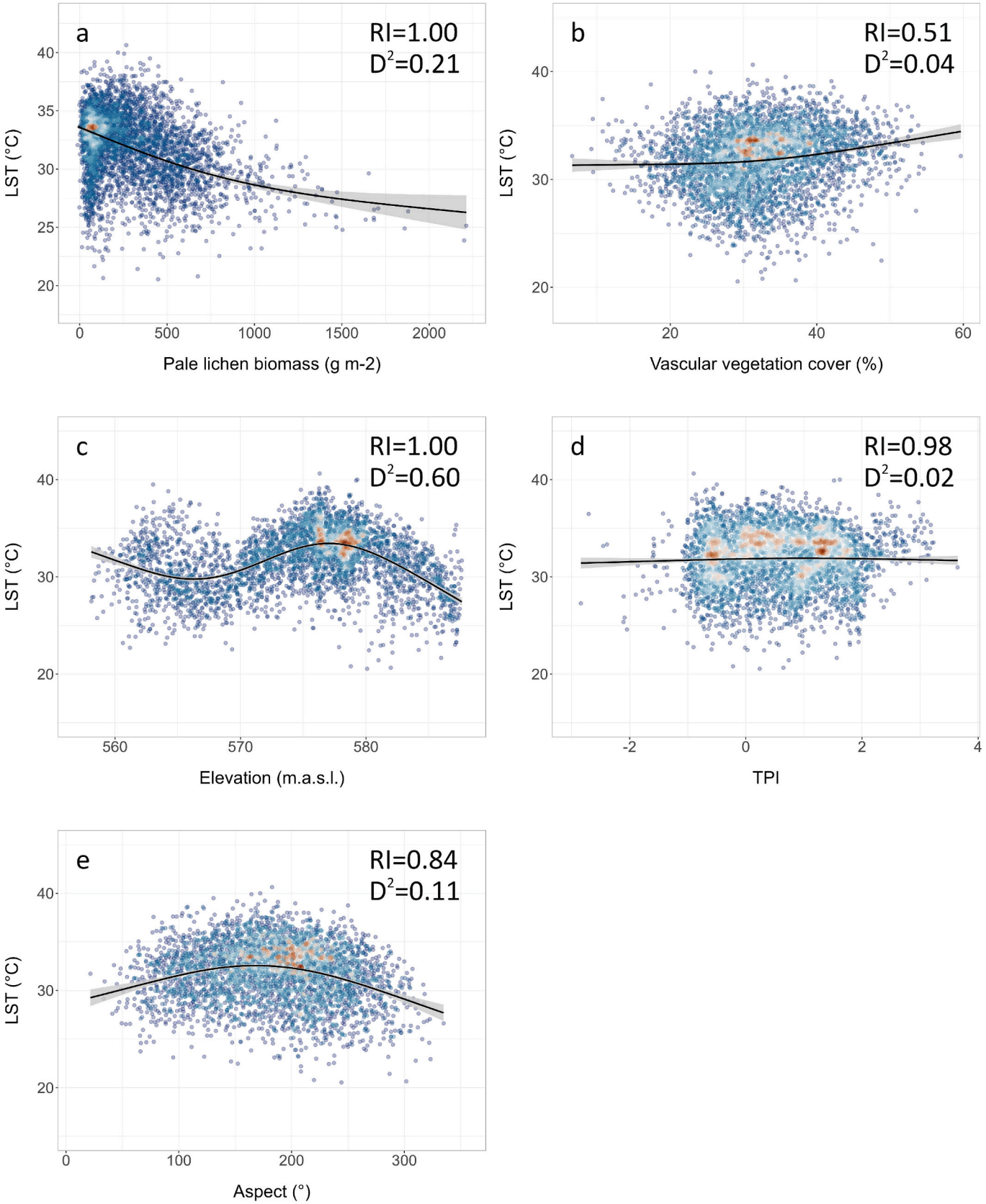

Fig. 4. Generalized Additive Models (GAMs) relating 5 environmental co-predictors and land surface temperature. Each plot represents the partial effects of pale lichen biomass (a), vascular vegetation cover (b), elevation (c), TPI (d), and aspect (e) on LST. The GAMs were calculated using UAV-derived data corresponding to the transect site. D^2: Partial deviance explained. RI: Relative importance. TPI: Topographic Position Index. LST: Land surface temperature.

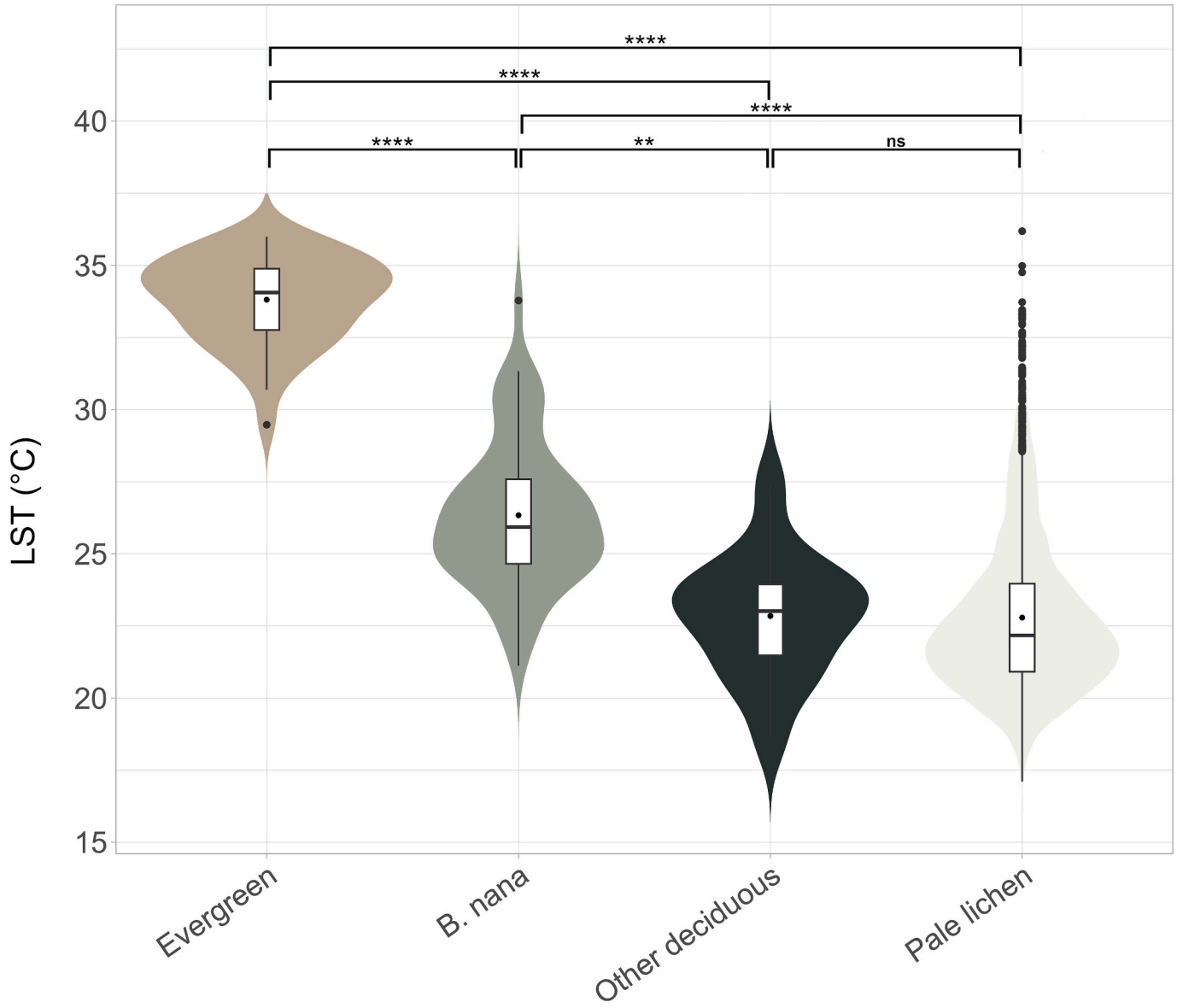

Fig. 5. Violin plots showing the average land surface temperature values (LST) for each plant and lichen group. The black dots inside the boxplot represent the mean LST value, while the curves on each side of the boxplots indicate the kernel density estimate of hexbins. Asterisks indicate statistical differences between plant functional and taxonomical groups, as indicated by the Games-Howell tests (ns = $p > 0.05$, * = $p \leq 0.05$, ** = $p \leq 0.01$, *** = $p \leq 0.001$, **** = $p \leq 0.0001$).

We argue the temporal scale of assessment partially explains the differences in the explanatory power between the UAV-scale and L8-scale modes. We retrieved LST readings at the transect site on a single-date 24-ha UAV flight. Within this restricted timeframe, factors such as atmospheric conditions, wind speed and direction, and radiance, and sensor-related issues such as stability of the thermal readings and self-heating, could significantly affect the LST measurements, masking the effects of topography and vegetation (Elfarkh et al., 2023; Kelly et al., 2019). However, it is worth noting that the UAV LST readings showed a small departure from the 10 years LST mean (Fig. S.3). In addition, it has been stated that rapid variations in LST due to local meteorological and environmental factors introduce within-flight uncertainty in UAV surveys (Elfarkh et al., 2023). This effect is likely amplified by the very high spatial resolution of the thermal images collected (16 cm per pixel in this study). On the other hand, the satellite datasets we used in this study are temporally aggregated as the summer (July–August) mean of all available and clean LST scenes, smoothing out the effects of single-date or single-year readings in seasonal estimates (Attiah et al., 2023; Carrasco et al., 2019).

Regardless of its intensity, the effect of pale lichen biomass on LST is consistent across spatial scales. Our observations align well with previously published research on the relationship between pale lichens and albedo. At plot scales, Finne et al. (2023) recently found that a higher coverage of ecorticate light-coloured lichens was associated to higher albedo, measuring a maximum value of 0.389, which is the highest broadband albedo recorded for a vegetated surface ever. At the landscape scale, Cohen et al. (2013) used MODIS data to unveil higher albedo values on the Norwegian side of the fence (characterised by higher pale lichen biomass) during the snow-free season. Here, we confirm that dense pale lichen mats have an essential role in regulating microclimate.

Among the set of co-predictors, elevation entailed the highest RI and D^2 in both local-scale and landscape-scale GAM models. This is not surprising, considering that in treeless tundra hills, soils at higher elevations are commonly dryer due to less snow accumulation during wintertime, a higher degree of wind exposition, and thinner soils (Kemppinen et al., 2017; Aalto et al., 2022). These environmental gradients combined with higher radiation and surface warming explain the

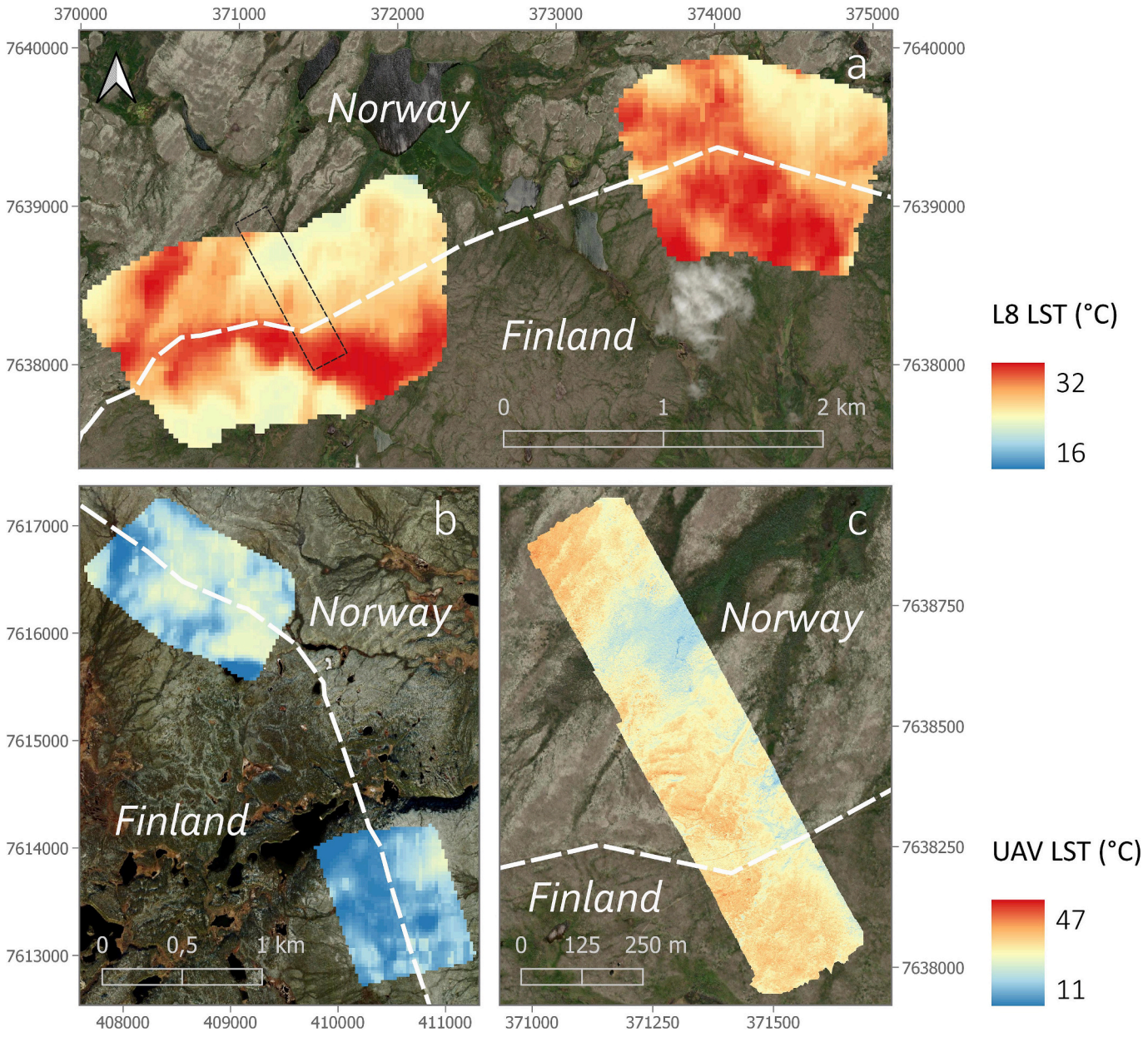

Fig. 6. Land surface temperature (LST) measured using Landsat-8 imagery, with a spatial resolution of 30 m per pixel, aggregated over a period of 10 years (2013–2023) at Jávrrešduottar (a) and Sieiddečearru (b). To facilitate visualization, Landsat images were cropped to the extent of the UAV survey areas. At the UAV transect site, thermal imagery was collected on 29/06/2023 with a spatial resolution of 16 cm per pixel. The border fence is shown as a dashed white line. Background images: ESRI Satellite World Imagery.

effect of elevation on LST, clearly visible on the landscape-scale model.

The landscape-scale model also unveiled clear differences between sites, with the Sieiddečearru GAM, explaining only 26.5 % of the total deviance (65.8 % at Jávrrešduottar), potentially indicating the influence of site-specific characteristics. We attribute these differences to the rather homogeneous and subtle environmental gradients that characterize Sieiddečearru site, which may be not adequately captured by the L8-derived LST, suggesting a potential spatial scale mismatch between UAV and satellite datasets. Both elevation and pale lichen biomass show a much higher variability in Jávrrešduottar (581.61 ± 17.55 m average elevation and 284.76 ± 183.55 g m^{-2} average pale lichen biomass) than in Sieiddečearru (488.70 ± 10.51 m average elevation and 162.22 ± 67.83 g m^{-2} average pale lichen biomass).

5.1. LST differences between plant functional and taxonomical groups

At the local scale, the UAV models unveiled a clear LST gradient from *evergreen* (avg. LST = 33.81 °C) to pale lichen-dominated areas, with pale lichens showing an average LST of 22.79 °C, just below 22.84 °C corresponding to *B. nana*. This indicates that at the UAV transect site, the overall surface cooling effect of pale lichen species was significantly higher than that of vascular vegetation, with the exception of *B. nana*. The higher LST of *evergreen shrubs* observed in our study can be attributed to differences in albedo and the structural configuration and leaf architecture of common species, such as *E. nigrum, Phyllodoce caerulea*, and *Calluna vulgaris*. In an experimental setting, Reinhardt et al. (2022) showed how a stepwise replacement of pale lichen species by *E. nigrum* led to a significant decrease in albedo. Moreover, Gersony et al. (2016) showed large differences in leaf surface temperatures among arctic tundra plants, with *E. nigrum* having comparatively higher leaf

Table 4
Results of GAMs assessing the effect of nine smooth terms on L8-derived LST for Jávrrešduottar and Sieiddečearru. The model summary includes the total percentage of deviance explained (D^2), the F statistic the relative importance of each smooth term (RI), and the partial deviance explained by each predictor (partial D^2). Predictors are shown as GAM smooth terms. TWI: Topographic Wetness Index, TPI: Topographic Position Index. RI: Relative importance. Significant contributions of smooth terms are highlighted with asterisks, where * indicates significant contribution at the 0.05 level, ** indicates significant contribution at the 0.01 level, *** indicates significant contribution at the 0.001 level, and **** indicates significant contribution at the 0.0001 level.

Jávrrešduottar					Sieiddečearru			
Smooth terms	F value	pv	RI	Partial D^2 (%)	F value*	pv	RI	Partial D^2 (%)
s(lichen biomass)	18.84	****	1.00	32.55	2.21	**	0.54	4.68
s(lichen cover)	–	–	–	–	5.39	****	0.62	15.48
s(vegetation cover)	1.06	**	0.59	5.59	9.85	****	0.86	7.06
s(aspect)	17.04	****	1.00	2.16	39.04	****	0.99	54.70
s(twi)	–	–	–	–	–	–	0.98	–
s(tpi)	–	–	–	–	6.31	****	0.81	8.00
s(distance to water)	–	–	–	–	3.83	****		3.32
s(soil cover)	2.66	***	0.53	4.49	7.58	****	0.95	6.76
s(elevation)	110.91	****	1.00	55.21	–	–	–	–
Overall deviance explained	65.8 %				26.50 %			

*The F value evaluates the significance of each smooth term in the model, calculated as the ratio of the mean square of the model to the mean square of the residuals.

temperatures. The authors attributed this to the low structural height and complexity, as well as the low leaf-level stomatal conductance and evaporative cooling of evergreen shrubs in tundra. *E. nigrum* thermal traits could also explain the increase in LST alongside increases in vascular vegetation fractional cover in both the local and landscape-scale GAMs (Figs. 4 and 7), as the vascular vegetation at our study sites is predominantly characterised by *E. nigrum.* Regarding the lower LST in *B. nana* and *other deciduous,* earlier studies have shown that the temperature of deciduous shrubs leaves is largely coupled to the temperature of the atmosphere, due to higher and more complex canopies (Lambers et al., 2008; Gersony et al., 2016). This in combination with higher stomatal conductance may explain the lower surface temperatures associated to these vascular plant groups. Although low-lying lichen mats are likely to not be subject to the temperature-homogenizing effect that eddies have on tall deciduous shrubs, their very high albedo (Finne et al., 2023) likely plays a key role in regulating LST.

At the landscape scale, we aggregated the overall vascular vegetation fractional cover map within the L8 pixels, thereby comparing LST between dense lichen mats and vascular plant vegetation on a monthly (July–August) basis throughout 10 years. Mann-Whitney *U* tests indicated a significantly higher LST in pixels dominated by vascular plant vegetation than in those characterised by dense pale lichen mats in almost all summer months under analysis, highlighting the cooling effect of pale lichens at the landscape scale. This observation also confirms the pattern observed at the local scale (Fig. 4).

Although this study highlights the benefits of combining UAV and satellite platforms, there are still shortcomings associated with the nature of UAV data collection. The representativity of single-date and single-time LST acquisition flights is limited, especially considering the sensitivity of LST readings to local weather conditions, clouds shadows, and other local-scale dynamics. Repeated UAV surveys at fixed temporal intervals over the snow-free season could provide a better overview of LST dynamics over lichen mats. However, in remote locations such as the Arctic tundra, systematic surveys are largely limited by logistic constraints and the rapidly changing weather conditions. To overcome these limitations, future research should explore the possibilities of spatial downscaling of satellite-derived LST observations to the spatial resolution of very high-resolution satellite data such as the PlanetScope constellations, or the High Spatial Resolution (HSR-LST) approach (Abunnasr and Mhawej, 2023).

The integration of high-resolution UAV and satellite remote sensing provides powerful tools for managing tundra ecosystems. Monitoring pale lichen biomass, closely linked to land surface temperature regulation, offers an early indicator of ecological change. Land managers can take advantage of these techniques to detect shifts in lichen cover and thermal regimes that may signal stress on the ecosystem, enabling adaptive management strategies and promoting ecosystem resilience.

6. Conclusions

Our study elucidated the role of pale lichen biomass in modulating LST dynamics in tundra ecosystems. By integrating field observations with a multi-scale remote sensing analysis, we provided empirical evidence for the cooling effect of pale lichen cover, highlighting its importance in shaping thermal regimes at both local and regional scales. In heath tundra ecosystems characterised by low-growth vegetation, increases in pale lichen biomass led to decreases in LST, although this effect is clearer at the landscape scale. Site-level landscape characteristics may also play a role in discerning LST dynamics, as the links between ecosystem structure and LST may not be evident at structurally homogeneous sites.

The use of UAV data allowed us to accurately predict pale lichen biomass at a centimetre-scale, and subsequently link it with LST measurements. This highlights the need for UAV-derived models that are able to capture the heterogenous and fine-scale structure of tundra ecosystems. More importantly, we emphasize the effectiveness of combining UAV and satellite data, therefore maximizing the benefits from the spatial and temporal scales provided by both platforms. Further research focusing on the mechanistic drivers of pale lichen-LST interactions will enhance our understanding of tundra ecosystem dynamics and inform effective conservation strategies in the face of climate change.

CRediT authorship contribution statement

Miguel Villoslada: Writing – review & editing, Writing – original draft, Visualization, Validation, Supervision, Methodology, Investigation, Formal analysis, Data curation, Conceptualization. **Thaísa Bergamo:** Writing – review & editing, Writing – original draft, Visualization, Validation, Methodology, Formal analysis, Data curation, Conceptualization. **Tiina Kolari:** Writing – review & editing, Writing – original draft, Methodology, Formal analysis. **Rasmus Erlandsson:** Writing – review & editing, Writing – original draft, Data curation. **Pasi Korpelainen:** Data curation. **Aleksi Räsänen:** Writing – review & editing, Writing – original draft, Data curation. **Teemu Tahvanainen:** Writing – review & editing, Data curation. **Hans Tømmervik:** Writing – review & editing, Data curation. **Tarmo Virtanen:** Writing – review & editing, Data curation. **Emelie Winquist:** Writing – review & editing, Data curation. **Timo Kumpula:** Writing – review & editing, Writing – original draft, Resources, Funding acquisition, Data curation.

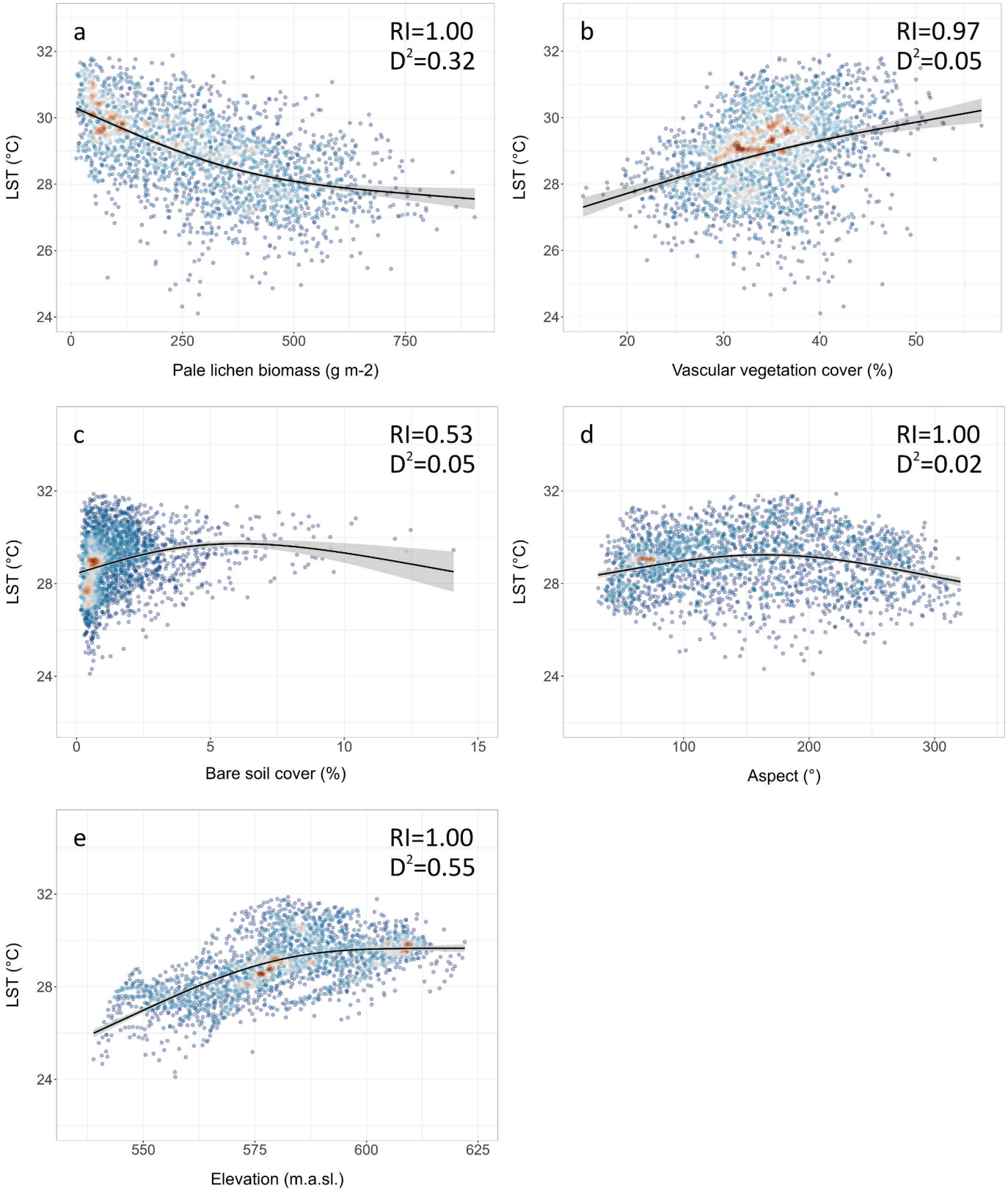

Fig. 7. Generalized Additive Models (GAMs) relating 5 environmental predictors and land surface temperature. Each plot represents the partial effects of pale lichen biomass (a), vascular vegetation cover (b), bare soil cover (c), aspect (d), and elevation (e) on LST. The GAMs were calculated using Landsat 8 LST and UAV-derived smooth terms at the Jávrrešduottar study site. D^2 = Partial deviance explained. RI: Relative Importance. LST: Land surface temperature.

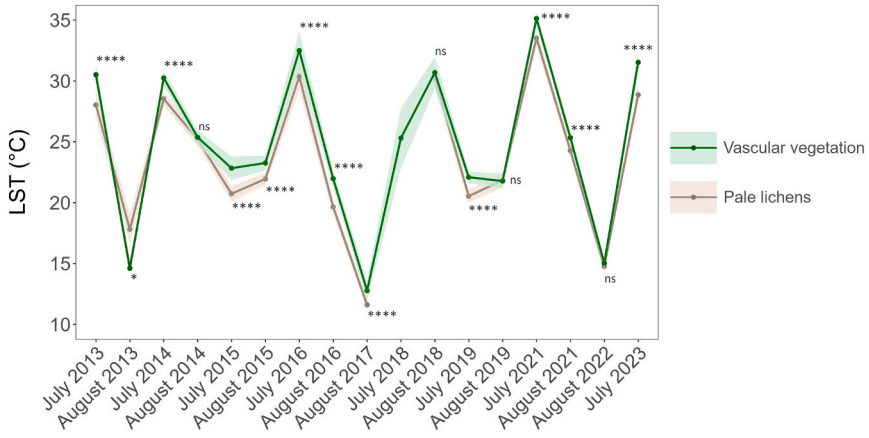

Fig. 8. Average land surface temperature derived from Landsat LST corresponding to the months of July and August within 10 years. The time series represents Landsat pixels dominated by pale lichens (light brown line) and vascular vegetation (green line). Pairwise comparisons in each month were assessed using a Mann-Whitney *U* test, where * indicates significant contribution at the 0.05 level, ** indicates significant contribution at the 0.01 level, *** indicates significant contribution at the 0.001 level, and **** indicates significant contribution at the 0.001 level. ns: not significant. Missing months are due to the lack of available Landsat scenes in the study areas.

Declaration of competing interest

The authors declare the following financial interests/personal relationships which may be considered as potential competing interests: Miguel Villoslada reports financial support was provided by Research Council of Finland. Miguel Villoslada reports financial support was provided by Horizon 2020 programme. If there are other authors, they declare that they have no known competing financial interests or personal relationships that could have appeared to influence the work reported in this paper.

Acknowledgements

The authors would like to thank Viivi Lindholm, Yuwen Pang, and Ella Rauth for their assistance during the field data collection process. This work was supported by Academy of Finland LANDMOD project (project nr: 330319) and EU Horizon 2020 CHARTER project (project nr: 2020 869471).

Appendix A. Supplementary data

Supplementary data to this article can be found online at https://doi.org/10.1016/j.scitotenv.2025.178982.

Data availability

Data will be made available on request.

References

Aalto, J., Tyystjärvi, V., Niittynen, P., Kemppinen, J., Rissanen, T., Gregow, H., Luoto, M., 2022. Microclimate temperature variations from boreal forests to the tundra. Agric. For. Meteorol. 323, 109037. https://doi.org/10.1016/j.agrformet.2022.109037.

Aartsma, P., Asplund, J., Odland, A., Reinhardt, S., Renssen, H., 2020. Surface albedo of alpine lichen heaths and shrub vegetation. Arctic, Antarctic, and Alpine Research 52 (1), 312–322.

Abunnasr, Y., Mhawej, M., 2023. Fully automated land surface temperature downscaling based on RGB very high spatial resolution images. City and Environment Interactions 19, 100110. https://doi.org/10.1016/j.cacint.2023.100110.

Akujärvi, A., Hallikainen, V., Hyppönen, M., Mattila, E., Mikkola, K., Rautio, P., 2014. Effects of reindeer grazing and forestry on ground lichens in Finnish Lapland. Silva Fennica 48 (3). https://doi.org/10.14214/sf.1153.

Armstrong, R.A., 2017. Adaptation of lichens to extreme conditions. Plant adaptation strategies in changing environment 1–27.

Asplund, J., Wardle, D.A., 2017. How lichens impact on terrestrial community and ecosystem properties. Biol. Rev. 92 (3), 1720–1738. https://doi.org/10.1111/brv.12305.

Attiah, G., Kheyrollah Pour, H., Scott, K.A., 2023. Lake surface temperature retrieved from Landsat satellite series (1984 to 2021) for the north slave region. Earth System Science Data 15 (3), 1329–1355. https://doi.org/10.5194/essd-15-1329-2023.

Barboza, F.R., Kotta, J., Weinberger, F., Jormalainen, V., Kraufvelin, P., Molis, M., Wahl, M., 2019. Geographic variation in fitness-related traits of the bladderwrack Fucus vesiculosus along the Baltic Sea-North Sea salinity gradient. Ecol. Evol. 9 (16), 9225–9238. https://doi.org/10.1594/PANGAEA.899902.

Barták, M., Hájek, J., Orekhova, A., Villagra, J., Marín, C., Palfner, G., and Casanova-Katny, A. (2021). Inhibition of primary photosynthesis in desiccating Antarctic lichens differing in their photobionts, thallus morphology, and spectral properties. Microorganisms, 9(4), 818. doi:https://doi.org/10.3390/microorganisms9040818.

Barton, K., Barton, M.K., 2015. Package 'mumin'. Version 1 (18), 439.

Bennett, K.E., Miller, G., Busey, R., Chen, M., Lathrop, E.R., Dann, J.B., Wilson, C.J., 2021. Spatial Patterns of Snow Distribution for Improved Earth System Modelling in the Arctic (Cryosphere. doi).

Beringer, J., Chapin III, F.S., Thompson, C.C., McGuire, A.D., 2005. Surface energy exchanges along a tundra-forest transition and feedbacks to climate. Agric. For. Meteorol. 131 (3–4), 143–161. https://doi.org/10.1016/j.agrformet.2005.05.006.

Bjerke, J.W., Bokhorst, S., Zielke, M., Callaghan, T.V., Bowles, F.W., Phoenix, G.K., 2011. Contrasting sensitivity to extreme winter warming events of dominant sub-Arctic heathland bryophyte and lichen species. J. Ecol. 99 (6), 1481–1488.

Bjerke, J.W., Magnussen, K., Bright, R.M., Navrud, S., Erlandsson, R., Finne, E.A., Tømmervik, H., 2024. Synergies and trade-offs between provisioning and climate-regulating ecosystem services in reindeer herding ecosystems. Sci. Total Environ. 171914. https://doi.org/10.1016/j.scitotenv.2024.171914.

Bruun, H.H., Moen, J., Virtanen, R., Grytnes, J.A., Oksanen, L., Angerbjörn, A., 2006. Effects of altitude and topography on species richness of vascular plants, bryophytes and lichens in alpine communities. J. Veg. Sci. 17 (1), 37–46.

Burnham, K.P., Anderson, D.R., 2002. Model Selection and Multimodel Inference: A Practical Information-Theoretic Approach. Springer, New York, NY, p. 488.

Carrasco, L., O'Neil, A.W., Morton, R.D., Rowland, C.S., 2019. Evaluating combinations of temporally aggregated Sentinel-1, Sentinel-2 and Landsat 8 for land cover mapping with Google earth engine. Remote Sens. (Basel) 11 (3), 288. https://doi.org/10.3390/rs11030288.

Chen, J., Zhang, M.Y., Wang, L., Shimazaki, H., Tamura, M., 2005. A new index for mapping lichen-dominated biological soil crusts in desert areas. Remote Sens. Environ. 96 (2), 165–175.

Chen, T., He, T., Benesty, M., Khotilovich, V., 2019. Package 'xgboost'. R version 90.

CloudCompare (version 2.12.4) [GPL software]. (2024). Retrieved from http://www.cloudcompare.org/.

Clausen, K.K., Stjernholm, M., Clausen, P., 2013. Grazing management can counteract the impacts of climate change-induced sea level rise on salt marsh-dependent waterbirds. J. Appl. Ecol. 50 (2), 528–537. https://doi.org/10.1111/1365-2664.12043.

Cohen, J., Pulliainen, J., Ménard, C.B., Johansen, B., Oksanen, L., Luojus, K., Ikonen, J., 2013. Effect of reindeer grazing on snowmelt, albedo and energy balance based on satellite data analyses. Remote Sens. Environ. 135, 107–117. https://doi.org/10.1016/j.rse.2013.03.029.

Cornelissen, J.H., Lang, S.I., Soudzilovskaia, N.A., During, H.J., 2007. Comparative cryptogam ecology: a review of bryophyte and lichen traits that drive biogeochemistry. Ann. Bot. 99 (5), 987–1001.

Crittenden, P.D., 2000. Aspects of the ecology of mat-forming lichens. Rangifer 20 (2–3), 127–139.

Datt, B., 1998. Remote sensing of chlorophyll a, chlorophyll b, chlorophyll a+ b, and total carotenoid content in eucalyptus leaves. Remote Sens. Environ. 66 (2), 111–121. https://doi.org/10.1016/S0034-4257(98)00046-7.

Debeffe, L., Maren Rivrud, I., Brekkum, Ø., Meisingset, E.L., Mysterud, A., 2017. Implications of the forage maturation hypothesis for activity of partially migratory male and female deer. Ecosphere 8 (12), e02050. https://doi.org/10.1002/ecs2.2050.

Den Herder, M., Kytöviita, M.M., Niemelä, P., 2003. Growth of reindeer lichens and effects of reindeer grazing on ground cover vegetation in a scots pine forest and a subarctic heathland in Finnish Lapland. Ecography 26 (1), 3–12. https://doi.org/10.1034/j.1600-0587.2003.03211.x.

Egelkraut, D., Barthelemy, H., Olofsson, J., 2020. Reindeer trampling promotes vegetation changes in tundra heathlands: results from a simulation experiment. J. Veg. Sci. 31 (3), 476–486. https://doi.org/10.1111/jvs.12871.

Elbert, W., Weber, B., Burrows, S., Steinkamp, J., Büdel, B., Andreae, M.O., Pöschl, U., 2012. Contribution of cryptogamic covers to the global cycles of carbon and nitrogen. Nat. Geosci. 5 (7), 459–462. https://doi.org/10.1038/ngeo1486.

Elfarkh, J., Johansen, K., Angulo, V., Camargo, O.L., McCabe, M.F., 2023. Quantifying within-flight variation in land surface temperature from a UAV-based thermal infrared camera. Drones 7 (10), 617. https://doi.org/10.3390/drones7100617.

Elmendorf, S.C., Henry, G.H., Hollister, R.D., Björk, R.G., Bjorkman, A.D., Callaghan, T. V., Wookey, P.A., 2012. Global assessment of experimental climate warming on tundra vegetation: heterogeneity over space and time. Ecol. Lett. 15 (2), 164–175.

Erlandsson, R., Bjerke, J.W., Finne, E.A., Myneni, R.B., Piao, S., Wang, X., Tømmervik, H., 2022. An artificial intelligence approach to remotely assess pale lichen biomass. Remote Sens. Environ. 280, 113201. https://doi.org/10.1016/j.rse.2022.113201.

Ermida, S.L., Soares, P., Mantas, V., Göttsche, F.M., Trigo, I.F., 2020. Google earth engine open-source code for land surface temperature estimation from the landsat series. Remote Sens. (Basel) 12 (9), 1471. https://doi.org/10.3390/rs12091471.

Fang, S., Yu, W., Qi, Y., 2015. Spectra and vegetation index variations in moss soil crust in different seasons, and in wet and dry conditions. Int. J. Appl. Earth Obs. Geoinf. 38, 261–266. https://doi.org/10.1016/j.jag.2015.01.018.

Finne, E.A., Bjerke, J.W., Erlandsson, R., Tømmervik, H., Stordal, F., Tallaksen, L.M., 2023. Variation in albedo and other vegetation characteristics in non-forested northern ecosystems: the role of lichens and mosses. Environ. Res. Lett. 18 (7), 074038. https://doi.org/10.1088/1748-9326/ace06d.

Finnish Meteorological Institute. Temperature and precipitation statistics from 1961 onwards. Retrieved 19 April, 2024, from https://en.ilmatieteenlaitos.fi/statistics-from-1961-onwards.

Fletcher, B.J., Gornall, J.L., Poyatos, R., Press, M.C., Stoy, P.C., Huntley, B., Phoenix, G. K., 2012. Photosynthesis and productivity in heterogeneous arctic tundra: consequences for ecosystem function of mixing vegetation types at stand edges. J. Ecol. 100 (2), 441–451. https://doi.org/10.1111/j.1365-2745.2011.01913.x.

Fraser, R.H., Lantz, T.C., Olthof, I., Kokelj, S.V., Sims, R.A., 2014. Warming-induced shrub expansion and lichen decline in the Western Canadian Arctic. Ecosystems 17, 1151–1168.

Fraser, R.H., Pouliot, D., van der Sluijs, J., 2022. UAV and high resolution satellite mapping of forage lichen (Cladonia spp.) in a rocky Canadian shield landscape. Can. J. Remote. Sens. 48 (1), 5–18. https://doi.org/10.1080/07038992.2021.1908118.

Gaare, E., and Tømmervik, H. 2000. Overvåking av lavbeiter i Finnmark. (monitoring of lichen grazing areas in Finnmark.) NINA Oppdragsmelding, 638: 1-31. Trondheim, Norway. (in Norwegian with English abstract).

Gersony, J.T., Prager, C.M., Boelman, N.T., Eitel, J.U., Gough, L., Greaves, H.E., Naeem, S., 2016. Scaling thermal properties from the leaf to the canopy in the Alaskan arctic tundra. Arctic, Antarctic, and Alpine Research 48 (4), 739–754. https://doi.org/10.1657/AAAR0016-013.

Gianelle, D., Vescovo, L., 2007. Determination of green herbage ratio in grasslands using spectral reflectance. Methods and ground measurements. Int. J. Remote Sens. 28 (5), 931–942. https://doi.org/10.1080/01431160500196398.

Gitelson, A.A., Kaufman, Y.J., Merzlyak, M.N., 1996. Use of a green channel in remote sensing of global vegetation from EOS-MODIS. Remote Sens. Environ. 58 (3), 289–298. https://doi.org/10.1016/S0034-4257(96)00072-7.

Gitelson, A., Merzlyak, M.N., 1994. Spectral reflectance changes associated with autumn senescence of Aesculus hippocastanum L. and Acer platanoides L. leaves. Spectral features and relation to chlorophyll estimation. J. Plant Physiol. 143 (3), 286–292. https://doi.org/10.1016/S0176-1617(11)81633-0.

Gitelson, A.A., Viña, A., Ciganda, V., Rundquist, D.C., Arkebauer, T.J., 2005. Remote estimation of canopy chlorophyll content in crops. Geophys. Res. Lett. 32 (8). https://doi.org/10.1029/2005GL022688.

Gorelick, N., Hancher, M., Dixon, M., Ilyushchenko, S., Thau, D., Moore, R., 2017. Google earth engine: planetary-scale geospatial analysis for everyone. Remote Sens. Environ. 202, 18–27. https://doi.org/10.1016/j.rse.2017.06.031.

He, J., Zhao, W., Li, A., Wen, F., Yu, D., 2019b. The impact of the terrain effect on land surface temperature variation based on Landsat-8 observations in mountainous areas. Int. J. Remote Sens. 40 (5–6), 1808–1827. https://doi.org/10.1080/01431161.2018.1466082.

He, L., Chen, W., Leblanc, S.G., Lovitt, J., Arsenault, A., Schmelzer, I., Pouliot, D., 2021. Integration of multi-scale remote sensing data for reindeer lichen fractional cover mapping in eastern Canada. Remote Sens. Environ. 267, 112731. https://doi.org/10.1016/j.rse.2021.112731.

He, L., Chen, W., Fraser, R.H., Schmelzer, I., Arsenault, A., Leblanc, S.G., Brodeur, A., 2024. Satellite-detected decreases in caribou lichen cover, Cladonia (Cladina) spp., over eastern Canada during the last three decades. For. Ecol. Manage. 556, 121753. https://doi.org/10.1016/j.foreco.2024.121753.

He, Z., Huo, S., Ma, C., Zhang, H., An, D., Xi, B., Wu, F., 2019a. The contributions of climate changes and human activities to long-term variations in lake sediments based on results from generalized additive models. Water Resour. Manag. 33, 1069–1085.

Helle, T., 1984. Foraging behaviour of semi-domesticated reindeer (Rangifer tarandus tarandus) in relation to snow in Finnish Lapland. Reports of Kevo Subarctic Research Station 19, 35–47.

Hodgetts, N. G. (1992). *Cladonia*: A Field Guide. Joint Nature Conservation Committee, Peterborough. ISBN 1 873701 08 X.

Hope, A., Engstrom, R., Stow, D., 2005. Relationship between AVHRR surface temperature and NDVI in Arctic tundra ecosystems. International Journal of Remote Sensing 26 (8), 1771–1776. https://doi.org/10.1080/01431160500043780.

Huete, A.R., 1988. A soil-adjusted vegetation index (SAVI). Remote Sens. Environ. 25 (3), 295–309. https://doi.org/10.1016/0034-4257(88)90106-X.

Ims Vistnes, I., Nellemann, C., 2008. Reindeer winter grazing in alpine tundra: impacts on ridge community composition in Norway. Arct. Antarct. Alp. Res. 40 (1), 215–224. https://doi.org/10.1657/1523-0430(07-001)[VISTNES]2.0.CO;2.

Inoue, T., Kudoh, S., Uchida, M., Tanabe, Y., Inoue, M., Kanda, H., 2017. Factors affecting water availability for high Arctic lichens. Polar Biol. 40, 853–862. https://doi.org/10.1007/s00300-016-2010-2.

Kalnay, E., Kanamitsu, M., Kistler, R., Collins, W., Deaven, D., Gandin, L., ... and Joseph, D. (2018). The NCEP/NCAR 40-year reanalysis project. In Renewable energy (pp. Vol1_146-Vol1_194). Routledge.

Jiang, Z., Huete, A.R., Didan, K., Miura, T., 2008. Development of a two-band enhanced vegetation index without a blue band. Remote Sens. Environ. 112 (10), 3833–3845. https://doi.org/10.1016/j.rse.2008.06.006.

Jin, H., Eklundh, L., 2014. A physically based vegetation index for improved monitoring of plant phenology. Remote Sens. Environ. 152, 512–525. https://doi.org/10.1016/j.rse.2014.07.010.

Kanaji, Y., Okazaki, M., Miyashita, T., 2017. Spatial patterns of distribution, abundance, and species diversity of small odontocetes estimated using density surface modeling with line transect sampling. Deep-Sea Res. II Top. Stud. Oceanogr. 140, 151–162. https://doi.org/10.1016/j.dsr2.2016.05.014.

Kelly, J., Kljun, N., Olsson, P.O., Mihai, L., Liljeblad, B., Weslien, P., Eklundh, L., 2019. Challenges and best practices for deriving temperature data from an uncalibrated UAV thermal infrared camera. Remote Sens. (Basel) 11 (5), 567. https://doi.org/10.3390/rs11050567.

Kemppinen, J., Niittynen, P., Riihimäki, H., Luoto, M., 2017. Modelling soil moisture in a high-latitude landscape using LiDAR and soil data. Earth Surf. Process. Landf. 43 (5), 1019–1031. https://doi.org/10.1002/esp.4301.

Kennedy, B., Pouliot, D., Manseau, M., Fraser, R., Duffe, J., Pasher, J., Olthof, I., 2020. Assessment of Landsat-based terricolous macrolichen cover retrieval and change analysis over caribou ranges in northern Canada and Alaska. Remote Sens. Environ. 240, 111694. https://doi.org/10.1016/j.rse.2020.111694.

Kivinen, S., Kaarlejärvi, E., Jylhä, K., Räisänen, J., 2012. Spatiotemporal distribution of threatened high-latitude snowbed and snow patch habitats in warming climate. Environ. Res. Lett. 7 (3), 034024. https://doi.org/10.1088/1748-9326/7/3/034024.

Kolari, T.H., Kumpula, T., Verdonen, M., Forbes, B.C., Tahvanainen, T., 2019. Reindeer grazing controls willows but has only minor effects on plant communities in Fennoscandian oroarctic mires. Arctic, Antarctic, and Alpine Research 51 (1), 506–520. https://doi.org/10.1080/15230430.2019.1679940.

Kopecký, M., Macek, M., and Wild, J. (2021). Topographic wetness index calculation guidelines based on measured soil moisture and plant species composition. Sci. Total Environ., 757, 143785.- doi:https://doi.org/10.1016/j.scitotenv.2020.143785.

Kumpula, J., Colpaert, A., 2007. Snow conditions and usability value of pastureland for semi-domesticated reindeer (Rangifer tarandus tarandus) in northern boreal forest area. Rangifer 27 (1). https://doi.org/10.7557/2.27.1.171.

Kross, A., McNairn, H., Lapen, D., Sunohara, M., Champagne, C., 2015. Assessment of RapidEye vegetation indices for estimation of leaf area index and biomass in corn and soybean crops. Int. J. Appl. Earth Obs. Geoinf. 34, 235–248. https://doi.org/10.1016/j.jag.2014.08.002.

Kumpula, T., 2006. Very high resolution remote sensing data in reindeer pasture inventory in northern Fennoscandia. In: Forbes, B.C., Bölter, M., Müller-Wille, L., Hukkinen, J., Müller, F., Gunslay, N., Konstantinov, Y. (Eds.), Reindeer Management in Northernmost Europe: Ecological Studies, vol. 184. Springer, pp. 167–185.

Lai, J., Tang, J., Li, T., Zhang, A., Mao, L., 2024. Evaluating the relative importance of predictors in generalized additive models using the gam. Hp R package. Plant Diversity. https://doi.org/10.1016/j.pld.2024.06.002.

Lambers, H., Chapin, F.S., Pons, S., 2008. Plant Physiological Ecology. Springer, New York.

Maguigan, M., Rodgers, J., Dash, P., Meng, Q., 2016. Assessing net primary production in montane wetlands from proximal, airborne, and satellite remote sensing. Adv. Remote Sens. 05 (02), 118–130. https://doi.org/10.4236/ars.2016.52010.

Malakar, N.K., Hulley, G.C., Hook, S.J., Laraby, K., Cook, M., Schott, J.R., 2018. An operational land surface temperature product for Landsat thermal data: methodology and validation. IEEE Trans. Geosci. Remote Sens. 56 (10), 5717–5735. https://doi.org/10.1109/TGRS.2018.2824828.

Man, Chuc Duc, Nguyen, Thuy Thanh, Bui, Hung Quang, Lasko, Kristofer, Nguyen, Thanh Nhat Thi, 2018. Improvement of land-cover classification over frequently cloud-covered areas using Landsat 8 time-series composites and an ensemble of supervised classifiers. International Journal of Remote Sensing 39 (4), 1243–1255. https://doi.org/10.1080/01431161.2017.1399477.

Mao, P., Ding, J., Jiang, B., Qin, L., Qiu, G.Y., 2022. How can UAV bridge the gap between ground and satellite observations for quantifying the biomass of desert shrub community? ISPRS J. Photogramm. Remote Sens. 192, 361–376. https://doi.org/10.1016/j.isprsjprs.2022.08.021.

Martínez Prentice, R., Villoslada Peciña, M., Ward, R.D., Bergamo, T.F., Joyce, C.B., Sepp, K., 2021. Machine learning classification and accuracy assessment from high-resolution images of coastal wetlands. Remote Sens. (Basel) 13 (18), 3669. https://doi.org/10.3390/rs13183669.

Meloche, J., Langlois, A., Rutter, N., McLennan, D., Royer, A., Billecocq, P., Ponomarenko, S., 2022. High-resolution snow depth prediction using random Forest algorithm with topographic parameters: a case study in the Greiner watershed. Nunavut. Hydrological Processes 36 (3), e14546. https://doi.org/10.1002/hyp.14546.

Muster, S., Langer, M., Abnizova, A., Young, K.L., Boike, J., 2015. Spatio-temporal sensitivity of MODIS land surface temperature anomalies indicates high potential for large-scale land cover change detection in Arctic permafrost landscapes. Remote Sens. Environ. 168, 1–12. https://doi.org/10.1016/j.rse.2015.06.017.

Naidoo, L., Van Deventer, H., Ramoelo, A., Mathieu, R., Nondlazi, B., Gangat, R., 2019. Estimating above ground biomass as an indicator of carbon storage in vegetated wetlands of the grassland biome of South Africa. Int. J. Appl. Earth Obs. Geoinf. 78, 118–129. https://doi.org/10.1016/j.jag.2019.01.021.

Nelson, P. R., Maguire, A. J., Pierrat, Z., Orcutt, E. L., Yang, D., Serbin, S., ... and Huemmrich, K. F. (2022). Remote sensing of tundra ecosystems using high spectral resolution reflectance: opportunities and challenges. *Journal of geophysical research:* Biogeosciences, 127(2), e2021JG006697. doi:https://doi.org/10.1029/2021JG006697.

Nill, L., Ullmann, T., Kneisel, C., Sobiech-Wolf, J., Baumhauer, R., 2019. Assessing spatiotemporal variations of Landsat land surface temperature and multispectral indices in the Arctic Mackenzie Delta region between 1985 and 2018. Remote Sens. (Basel) 11 (19), 2329. https://doi.org/10.3390/rs11192329.

Pannewitz, S., Schlensog, M., Green, T.A., Sancho, L.G., Schroeter, B., 2003. Are lichens active under snow in continental Antarctica? Oecologia 135, 30–38.

Qi, J., Chehbouni, A., Huete, A.R., Kerr, Y.H., Sorooshian, S., 1994. A modified soil adjusted vegetation index. Remote Sens. Environ. 48 (2), 119–126. https://doi.org/10.1016/0034-4257(94)90134-1.

Quillfeldt, P., Cherel, Y., Navarro, J., Phillips, R.A., Masello, J.F., Suazo, C.G., Bustamante, P., 2022. Variation among species and populations, and carry-over effects of winter exposure on mercury accumulation in small petrels. Front. Ecol. Evol. 10, 915199. https://doi.org/10.3389/fevo.2022.915199.

Räsänen, A., Virtanen, T., 2019. Data and resolution requirements in mapping vegetation in spatially heterogeneous landscapes. Remote Sens. Environ. 230, 111207. https://doi.org/10.1016/j.rse.2019.05.026.

Reinhardt, S., Aartsma, P., Skøyen, K., Renssen, H., 2022. Shrub encroachment interacts with environmental variation to reduce the albedo of alpine lichen heaths: an experimental study. Nord. J. Bot. 2022 (3). https://doi.org/10.1111/njb.03314.

Richardson, A.J., Everitt, J.H., 1992. Using spectral vegetation indices to estimate rangeland productivity. Geocarto Int. 7 (1), 63–69. https://doi.org/10.1080/10106049209354353.

Richardson, G., Leblanc, S.G., Lovitt, J., Rajaratnam, K., Chen, W., 2021. Leveraging AI to estimate caribou lichen in UAV orthomosaics from ground photo datasets. Drones 5 (3), 99. https://doi.org/10.3390/drones5030099.

Rouse, J.W., Haas, R.H., Schell, J.A., Deering, D.W., 1974. Monitoring vegetation systems in the great plains with ERTS proceeding. In: Third Earth Reserves Technology Satellite Symposium, Greenbelt: NASA SP-351, Vol. 30103017.

Schuur, E.A., Crummer, K.G., Vogel, J.G., Mack, M.C., 2007. Plant species composition and productivity following permafrost thaw and thermokarst in Alaskan tundra. Ecosystems 10, 280–292.

Simpson, G.L., 2018. Modelling palaeoecological time series using generalized additive models. https://doi.org/10.1101/322248.

Smith, M.W., Carrivick, J.L., Quincey, D.J., 2016. Structure from motion photogrammetry in physical geography. Prog. Phys. Geogr. 40 (2), 247–275. https://doi.org/10.1177/0309133331561580.

Sonesson, M., Callaghan, T.V., 1991. Strategies of survival in plants of the Fennoscandian tundra. Arctic 95–105.

Sörensen, R., Zinko, U., Seibert, J., 2006. On the calculation of the topographic wetness index: evaluation of different methods based on field observations. Hydrol. Earth Syst. Sci. 10 (1), 101–112. https://doi.org/10.5194/hess-10-101-2006.

Soudzilovskaia, N.A., van Bodegom, P.M., Cornelissen, J.H., 2013. Dominant bryophyte control over high-latitude soil temperature fluctuations predicted by heat transfer traits, field moisture regime and laws of thermal insulation. Funct. Ecol. 27 (6), 1442–1454.

Sripada, R.P., Heiniger, R.W., White, J.G., Meijer, A.D., 2006. Aerial color infrared photography for determining early in-season nitrogen requirements in corn. Agron. J. 98 (4), 968–977. https://doi.org/10.2134/agronj2005.0200.

Tømmervik, H., Bjerke, J.W., Gaare, E., Johansen, B., Thannheiser, D., 2012. Rapid recovery of recently overexploited winter grazing pastures for reindeer in northern Norway. Fungal Ecol. 5 (1), 3–15. https://doi.org/10.1016/j.funeco.2011.08.002.

Ullah, S., Si, Y., Schlerf, M., Skidmore, A.K., Shafique, M., Iqbal, I.A., 2012. Estimation of grassland biomass and nitrogen using MERIS data. Int. J. Appl. Earth Obs. Geoinf. 19, 196–204. https://doi.org/10.1016/j.jag.2012.05.008.

Van De Kerchove, R., Lhermitte, S., Veraverbeke, S., Goossens, R., 2013. Spatio-temporal variability in remotely sensed land surface temperature, and its relationship with physiographic variables in the Russian Altay Mountains. Int. J. Appl. Earth Obs. Geoinf. 20, 4–19. https://doi.org/10.1016/j.jag.2011.09.007.

Viana, D.S., Keil, P., Jeliazkov, A., 2022. Disentangling spatial and environmental effects: flexible methods for community ecology and macroecology. Ecosphere 13 (4), e4028. https://doi.org/10.1002/ecs2.4028.

Villoslada, M., Sipelgas, L., Bergamo, T.F., Ward, R.D., Reintam, E., Astover, A., Sepp, K., 2022. Multi-source remote sensing data reveals complex topsoil organic carbon dynamics in coastal wetlands. Ecol. Indic. 143, 109329. https://doi.org/10.1016/j.ecolind.2022.109329.

Villoslada, M., Ylänne, H., Juutinen, S., Kolari, T.H., Korpelainen, P., Tahvanainen, T., Kumpula, T., 2023. Reindeer control over shrubification in subarctic wetlands: spatial analysis based on unoccupied aerial vehicle imagery. Remote Sensing in Ecology and Conservation. https://doi.org/10.1002/rse2.337.

Vincini, M., Frazzi, E., D'alessio, P., Stafford, J.V., 2007. Comparison of narrow-band and broad-band vegetation indexes for canopy chlorophyll density estimation in sugar beet. Precis. Agric. 7, 189–196. https://doi.org/10.3920/978-90-8686-603-8.

Virtanen, T., Ek, M., 2014. The fragmented nature of tundra landscape. International Journal of Applied Earth Observation and Geoinformation 27, 4–12. https://doi.org/10.1016/j.jag.2013.05.010.

Weiss, A., 2001. Topographic position and landforms analysis. In: Poster Presentation, ESRI User Conference, San Diego, CA, 200.

Wood, S., Wood, M.S., 2015. Package 'mgcv'. R package version 1 (29), 729. https://doi.org/10.32614/CRAN.package.mgcv.

Xue, J., Anderson, M.C., Gao, F., Hain, C., Sun, L., Yang, Y., Schull, M., 2020. Sharpening ECOSTRESS and VIIRS land surface temperature using harmonized Landsat-sentinel surface reflectances. Remote Sens. Environ. 251, 112055.

Yang, D., Morrison, B.D., Hantson, W., Breen, A.L., McMahon, A., Li, Q., Serbin, S.P., 2021. Landscape-scale characterization of Arctic tundra vegetation composition, structure, and function with a multi-sensor unoccupied aerial system. Environ. Res. Lett. 16 (8), 085005. https://doi.org/10.1088/1748-9326/ac1291.

Zhang, H., Aldana-Jague, E., Clapuyt, F., Wilken, F., Vanacker, V., Van Oost, K., 2019a. Evaluating the potential of post-processing kinematic (PPK) georeferencing for UAV-based structure-from-motion (SfM) photogrammetry and surface change detection. Earth Surf. Dyn. 7 (3), 807–827. https://doi.org/10.5194/esurf-7-807-2019.

Zhang, H., Eziz, A., Xiao, J., Tao, S., Wang, S., Tang, Z., Fang, J., 2019b. High-resolution vegetation mapping using eXtreme gradient boosting based on extensive features. Remote Sens. (Basel) 11 (12), 1505. https://doi.org/10.3390/rs11121505.

Zhang, W., Qi, J., Wan, P., Wang, H., Xie, D., Wang, X., Yan, G., 2016. An easy-to-use airborne LiDAR data filtering method based on cloth simulation. Remote Sens. (Basel) 8 (6), 501. https://doi.org/10.3390/rs8060501.

Zhao, J., Cao, J., Tian, S., Chen, Y., Zhang, S., Wang, Z., Zhou, X., 2014. A comparison between two GAM models in quantifying relationships of environmental variables with fish richness and diversity indices. Aquat. Ecol. 48, 297–312. https://doi.org/10.1007/s10452-014-9484-1.

Zuur, A. F., Ieno, E. N., Walker, N. J., Saveliev, A. A., and Smith, G. M. (2009). Mixed effects models and extensions in ecology with R (Vol. 574, p. 574). New York: springer.